SUPPLEMENTARY INFORMATION

Spontaneous and self-oriented growth during chemical vapor epitaxy of single-crystalline MoS_2

Iryna Kandybka[1,2], Pawan Kumar[2]*, Henry Medina Silva[2]*, Benjamin Groven[2], Ankit Nalin Mehta[2], Yuanyuan Shi[2,▲], Quentin Smets[2], Tom Schram[2], Sreetama Banerjee[2], Cesar Javier Lockhart de la Rosa[2], Gouri Sankar Kar[2], Pierre Morin[2], Annelies Delabie[2,1]*

[1]*Department of Chemistry KU Leuven, Celestijnenlaan 200F, Leuven, 3001, Belgium*

[2]*imec, Kapeldreef 75, Leuven, 3001, Belgium*

Current address ▲ School of Microelectronics, University of Science and Technology of China (USTC), Jinzhai Road 96, Hefei, 230026, China

E-mail: Pawan.Kumar@imec.be; Henry.MedinaSilva@imec.be; Annelies.Delabie@imec.be

Note 1: MOCVD of MoS_2 from $Mo(CO)_6$ and H_2S

At the deposition temperature of 1000 °C, H_2S decomposes in the gas phase through the reversible reaction $H_2S \rightleftharpoons H_2 + S$ (Reaction 1).[1] H_2S and sulfur from the gas phase can adsorb on the surface, forming an S adatom. On the other hand, $Mo(CO)_6$ decomposes in the gas phase at the temperatures exceeding 250 °C, forming a Mo atom and carbonyl by-products.[2] Mo can react with H_2S (or S) in the gas phase, resulting in MoS_2. Alternatively, the generated Mo atom can adsorb on the surface, forming a Mo adatom. Both S and Mo adatoms can diffuse over the surface and aggregate with other adatoms to form nuclei or aggregate with already formed MoS_2 crystals. Sulfur adatoms can also desorb from the growth surface, diffuse in the gas phase, and adsorb again. In contrast, the desorption of Mo adatoms in this system has a low probability even at 1000 °C.[3] As a result, the deposition proceeds in mass transport limited regime, and precursor delivery rate of Mo determines the metal adsorption and diffusion kinetics on the surface (**Figure 3b**). Due to the much higher concentration of supplied S compared to Mo precursor species, MoS_2 growth rate and nucleation density is primarily governed by the adsorption and diffusion kinetics of the metal ad-species (**Figure S2**).

The adsorption rate can be defined as $R_{ads} = S \cdot F$ (Reaction 2), where S is a sticking coefficient, and F is a precursor flux. For the Mo atoms adsorbing on the sapphire surface, the sticking coefficient can be considered a constant, ignoring adsorption on MoS_2 crystals in the initial growth stage. Then, the

adsorption rate of Mo atoms is determined by the flux of Mo atoms to the surface, which in turn is controlled by the metal concentration in the chamber. Thus, a higher Mo concentration in the gas phase leads to a higher adsorption rate, more Mo adatoms on the surface and, therefore, higher deposition rate, consistent with Figure 2a and b.

Following classical nucleation theory, higher partial pressure of the metal precursor leads to the lower potential barrier for the heterogeneous nucleation.[4] Additionally, the higher metal concentration increases the probability of gas phase and surface aggregation, contributing to the higher areal density of MoS_2 crystals (Figure 3d). When $Mo(CO)_6$ concentration increases from 0.1 to 1.0 ppm, the maximal areal density of MoS_2 crystals also increases from $3.5 \cdot 10^2$ to $1.2 \cdot 10^3$ crystals/μm^2, respectively. As a result, the interdomain distance between crystals in the steady state decreases from 56 to 29 nm when $Mo(CO)_6$ concentration increases from 0.1 to 1.0, respectively.

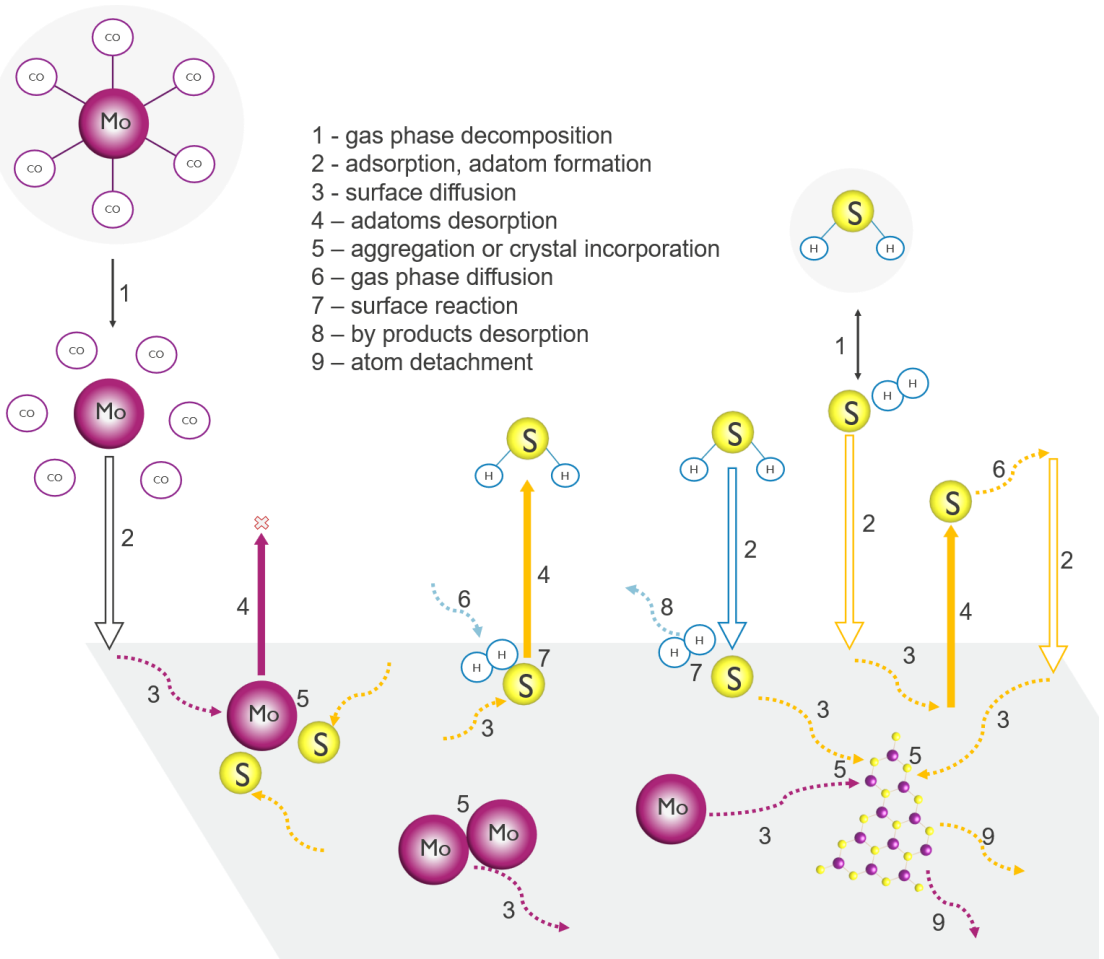

Figure S1. A schematic depicting the main processes occurring during MoS_2 CVD from $Mo(CO)_6$ and H_2S indicates the irreversible adsorption of Mo on the template's surface.

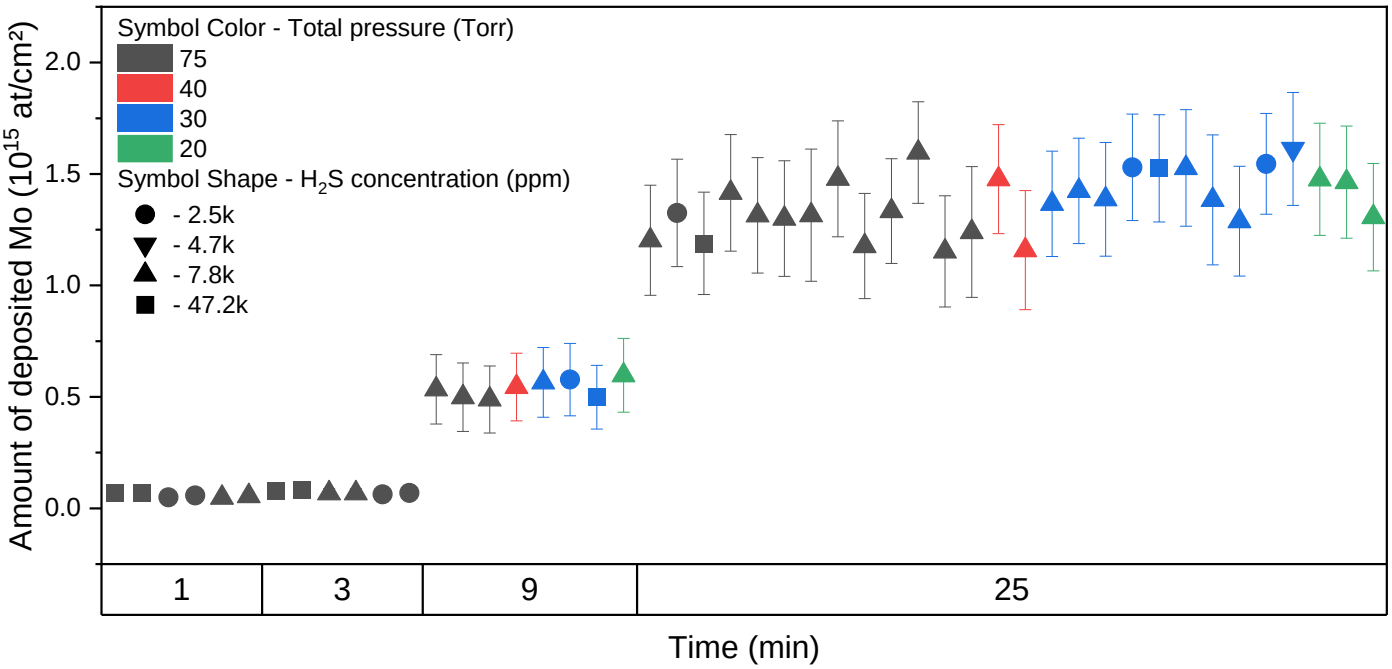

Figure S2. The metal precursor concentration determines the growth rate of MoS_2, as demonstrated by changing the total pressure and H_2S concentration, while keeping the $Mo(CO)_6$ concentration constant at 0.6 ppm. The amount of deposited Mo is determined by Rutherford backscattering spectrometry (RBS).

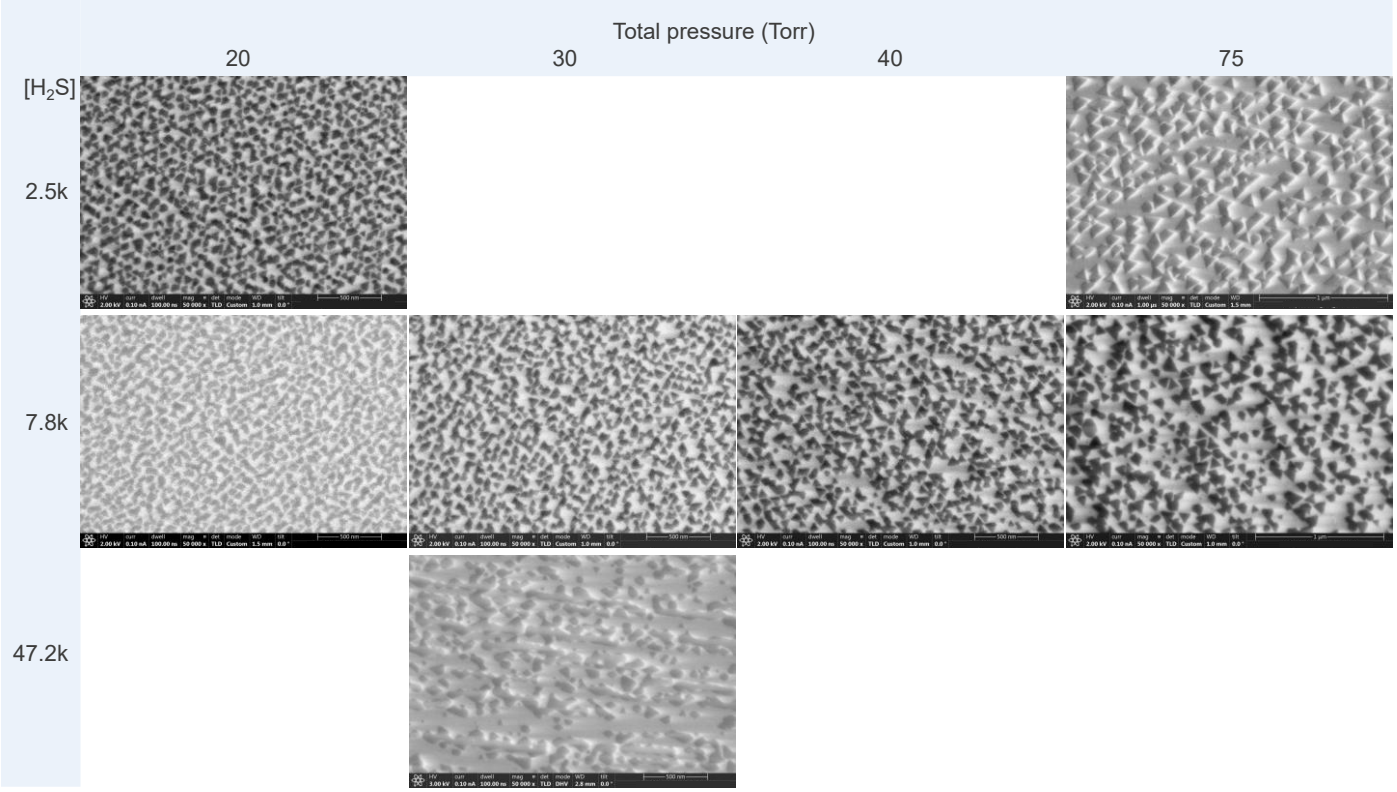

Figure S3. SEM images demonstrate the similar morphology of MoS_2 crystals deposited with a metal concentration of 0.6 ppm at different H_2S concentrations and total pressure. Very high H_2S concentration leads to topography-governed growth of the MoS_2 crystals, due to H_2S reactivity towards sapphire substrate and more pronounced sapphire surface reconstruction.

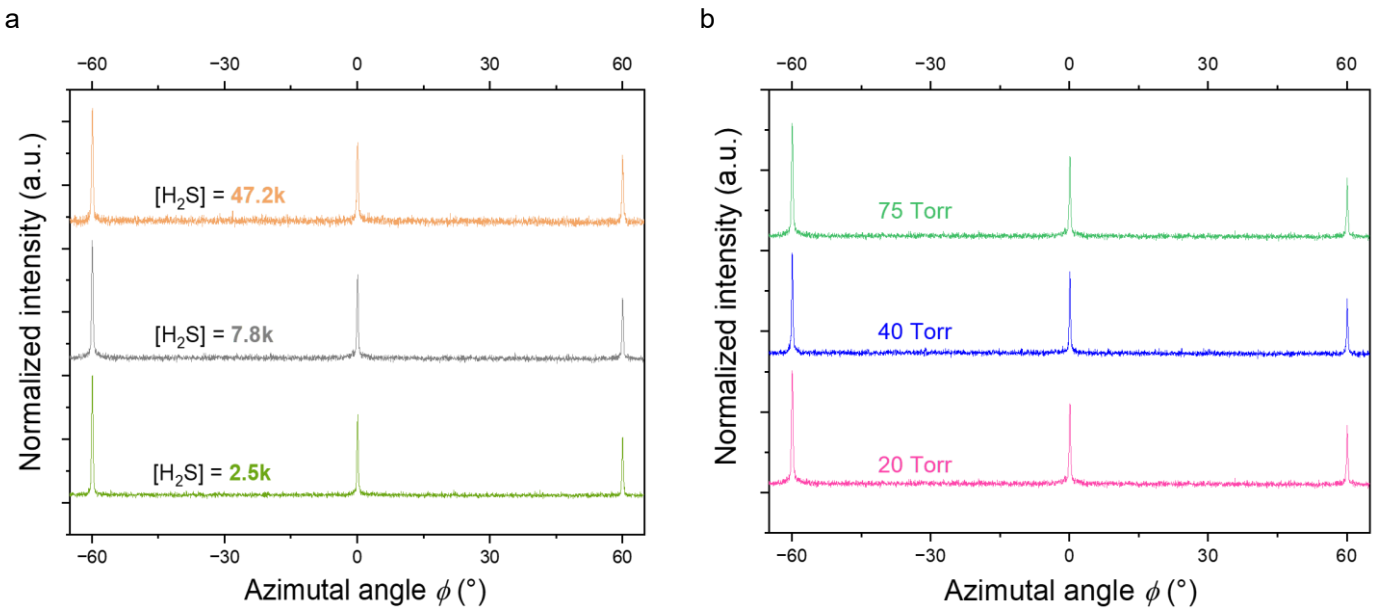

Figure S4. For MoS_2 crystals deposited with 0.6 ppm of $Mo(CO)_6$, we modify the total pressure in the chamber and the H_2S precursor concentration, keeping all the other process parameters the same. Changes in sulfur precursor concentration (a) and total pressure (b) do not affect the MoS_2 monolayer properties from an in-plane GI-XRD perspective.

Note 2: Bimodal MoS_2 crystal size distribution

A non-uniform crystal size distribution is characteristic for the MoS_2 crystals. At a higher metal precursor molar concentration of 1.0 ppm, the MoS_2 crystals exhibit a high areal density and begin to coalesce quickly during the deposition process, making it difficult to study the evolution of crystal size. At lower metal precursor concentrations, the deposition process is slower, allowing the evolution of crystal size to be investigated (**Figure S5**). In the initial growth stage, two peaks in the crystal size distribution are present: the small crystals peak ($S_{crystal}$) and the large crystals peak ($L_{crystal}$). On one hand, the $L_{crystal}$ peak shifts to the right during the deposition process, indicating a further increase in the size of large crystals. On the other hand, the $S_{crystal}$ peak remains in the same position and does not change with deposition time. Interestingly, at the lowest metal precursor concentration of 0.1 ppm, where the growth of the MoS_2 domains is slow enough, a size gap between the large and small crystals is observed as deposition time increases. Thus, the small crystals on average do not grow beyond the critical size of 25-35 nm and are present throughout the depostion process.

The observed bimodality in MoS_2 crystallite sizes suggests three possible scenarios during crystal growth, depending on the relative kinetics of atom attachment, detachment, and adatom diffusion. In the first scenario, most of the stable nuclei form at the beginning of the deposition process, some grow faster,

forming the large crystals, while others remain small. In this case, the small crystals continuously attach, release and exchange atoms though a surface-mediated process with the larger crystals, contributing to their growth. Simultaneously, the small crystals do not exceed their critical size. In the second scenario, the small crystals undergo constant consumption by giving away all of their atoms and then regenerating (renucleation). Lastly in the third scenario, the small crystals are not present during the deposition process itself but form during the cooling down stage from Mo adatoms on the surface when the temperature begins to decrease, limiting the diffusion length of those adatoms. In all proposed scenarios, the large crystals are the main constitutive part of the MoS_2 monolayer, establishing its properties.

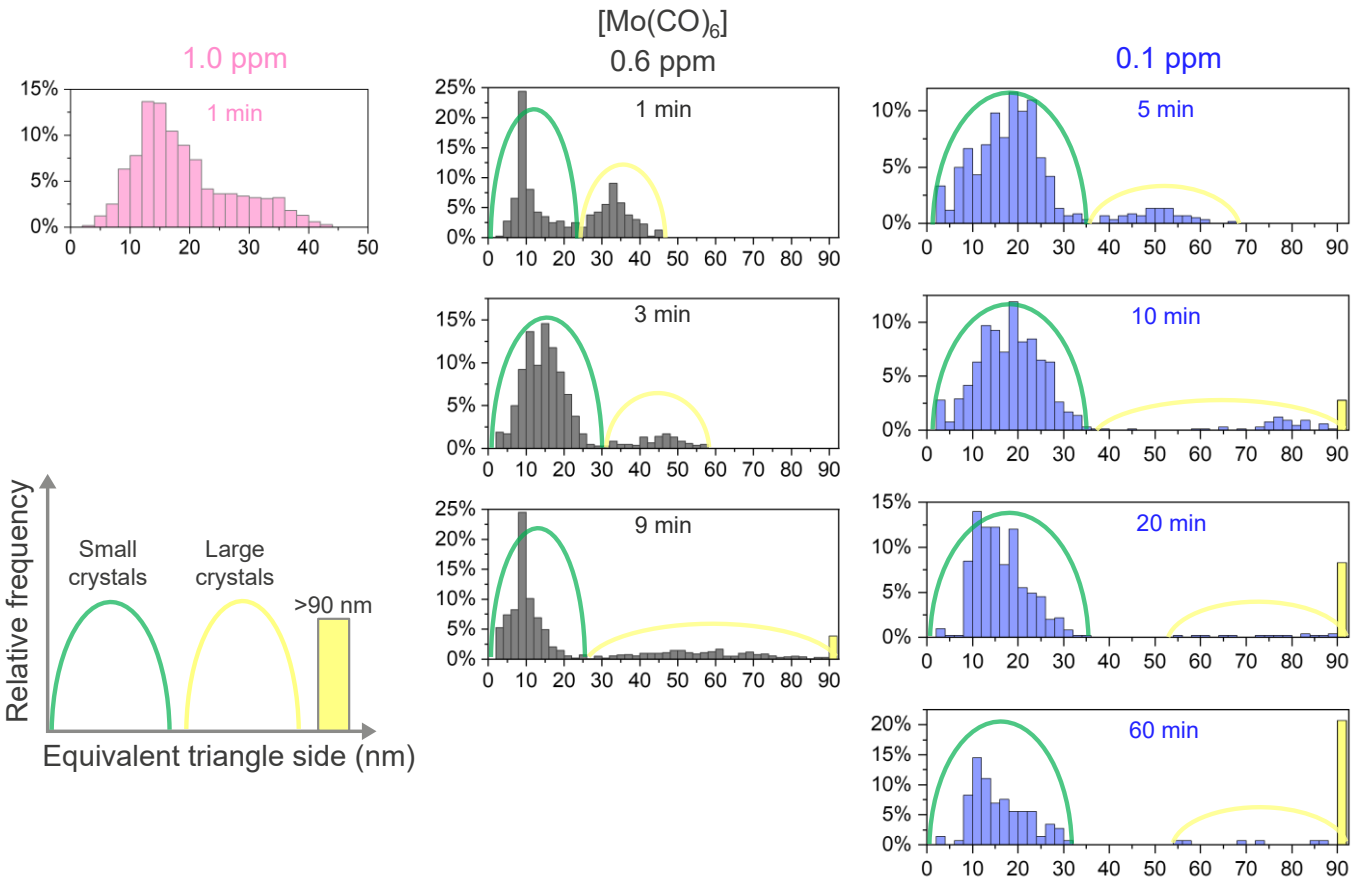

Figure S5. The bimodal MoS_2 crystal size distribution during the deposition process for $Mo(CO)_6$ concentration of 0.6 ppm and 0.1 ppm.

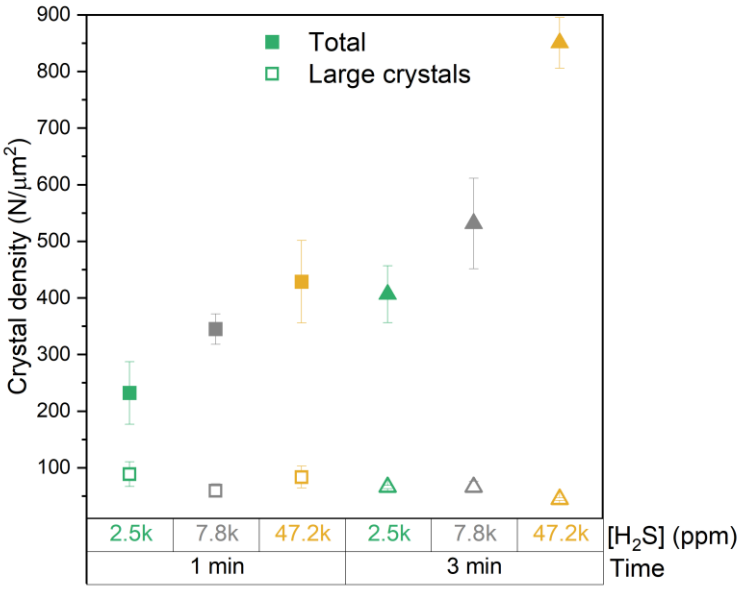

Figure S6. The MoS_2 crystal density increases early in the deposition process with the increase of the H_2S concentration, when deposited with 0.6 ppm of $Mo(CO)_6$. We hypothesize that interaction of H_2S/H_2 molecules with the sapphire substrate leads to surface defects formation. Around these surface defects, the nucleation probability of MoS_2 increases. However, the nucleation density increase is observed only for the small crystals, while the density of large crystals with an equivalent triangle side above 25-35 nm stays approximately the same. As the larger crystals dominate later in the deposition process, the closed MoS_2 monolayers free of misoriented domains, as confirmed by in plane GI-XRD (Figure S4).

Note 3: Sapphire template morphological change

The ambient environment significantly influences the reconstruction behavior of the sapphire surface (**Figure S7a**). When the substrate is annealed in an inert nitrogen (N_2) or hydrogen (H_2) environment at 1000°C for 30 minutes, only a slight change from the original surface morphology is observed. However, when annealing is performed in a hydrogen sulfide (H_2S) environment, a much more pronounced coalescence of terraces occurs, resulting in larger, more uniform surface areas. Interestingly, when the $Mo(CO)_6$ precursor is added to H_2S atmosphere during MOCVD and MoS_2 deposition is initiated, the sapphire surface modification proceeds differently compared to just the H_2S atmosphere. This indicates a coupled effect: on the one hand, the sapphire bulk crystallographic symmetry guides the MoS_2 orientation through van der Waals interactions, on the other hand, the growing MoS_2 crystals affects the way the sapphire surface reconstructs.

On the other hand, the orientation of isolated MoS_2 crystallites remains unchanged when the sapphire surface is pre-annealed in H_2S, indicating that potential sulfur-induced surface passivation does not influence the epitaxial alignment of MoS_2 crystals (Figure S7b).

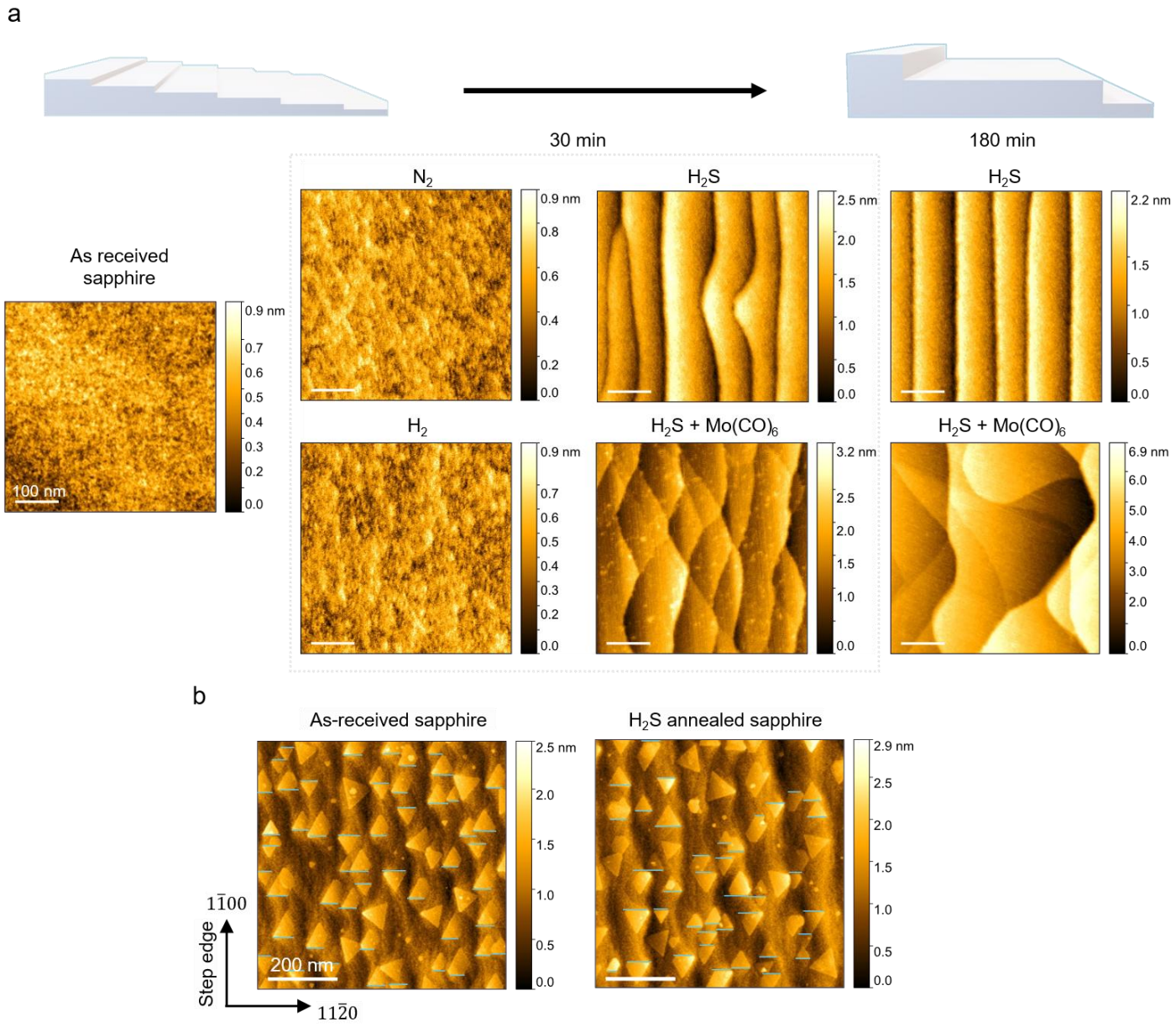

Figure S7. a, Changes of the sapphire surface depend on the chemicals present in the chamber during pretreatment at 1000 °C, as revealed by atomic force microscopy (AFM) images. For H_2S + $Mo(CO)_6$, MoS_2 is deposited on top of the sapphire surface and transferred prior to AFM imaging. **b**, The orientation of MoS_2 crystals is the same for as-received and H_2S-treated (30 min, 0.1 slm) sapphire. The deposition time is 30 minutes with 0.6 ppm of $Mo(CO)_6$.

Note 4: Crystal shape evolution with different metal precursor concentration

The presence of steps on the sapphire surface can affect the shape of MoS_2 crystals. The steps on sapphire surface with the step edge along the [1-100] crystallographic direction can be generated when the off-cut direction is the [11-20] A-axis. For the R0° epitaxial relationship between the sapphire c-plane and the MoS_2 crystals, the triangular crystals are oriented perpendicular to the step edge. If the terrace width is much shorter than the diffusion length of the metal adatoms on the surface, anisotropic diffusion can be initiated. [5] Here, we use off-A axis cut sapphire with a 1° off-axis cut angle and an initial terrace width of 12.4 nm, which further increases due to step coalescence. As a result, the MoS_2 crystals deposited with a metal precursor concentration of 0.1 ppm demonstrate anisotropic development of crystal facets, as we reported previously (**Figure S8**a) [5]. The crystal shape changes from triangular to diamond in a slow, step-by-step process, as depicted in Figure S3a. When the metal precursor concentration increases to 0.6 ppm, MoS_2 crystals shape follows the same anisotropic growth pathway as MoS_2 crystals at 0.1 ppm. However, at 0.6 ppm, different stages of crystal development coexist simultaneously, in contrast to step-by-step evolution observed at the lower metal precursor concentration (Figure S8b). Here, the higher adsorption rate causes the non-homogeneous distribution of metal adatoms on the surface. These adatoms exhibit anisotropic surface diffusion because of the steps present on the surface and sapphire surface reconstruction. As a result, facets of different crystals develop at varying speeds, as indicated by the different stages of shape evolution. When the metal concentration is further increased to 1.0 ppm, crystal coalescence starts very early in the deposition process because of high nucleation density, and no change in MoS_2 crystal shape is observed (Figure S8c).

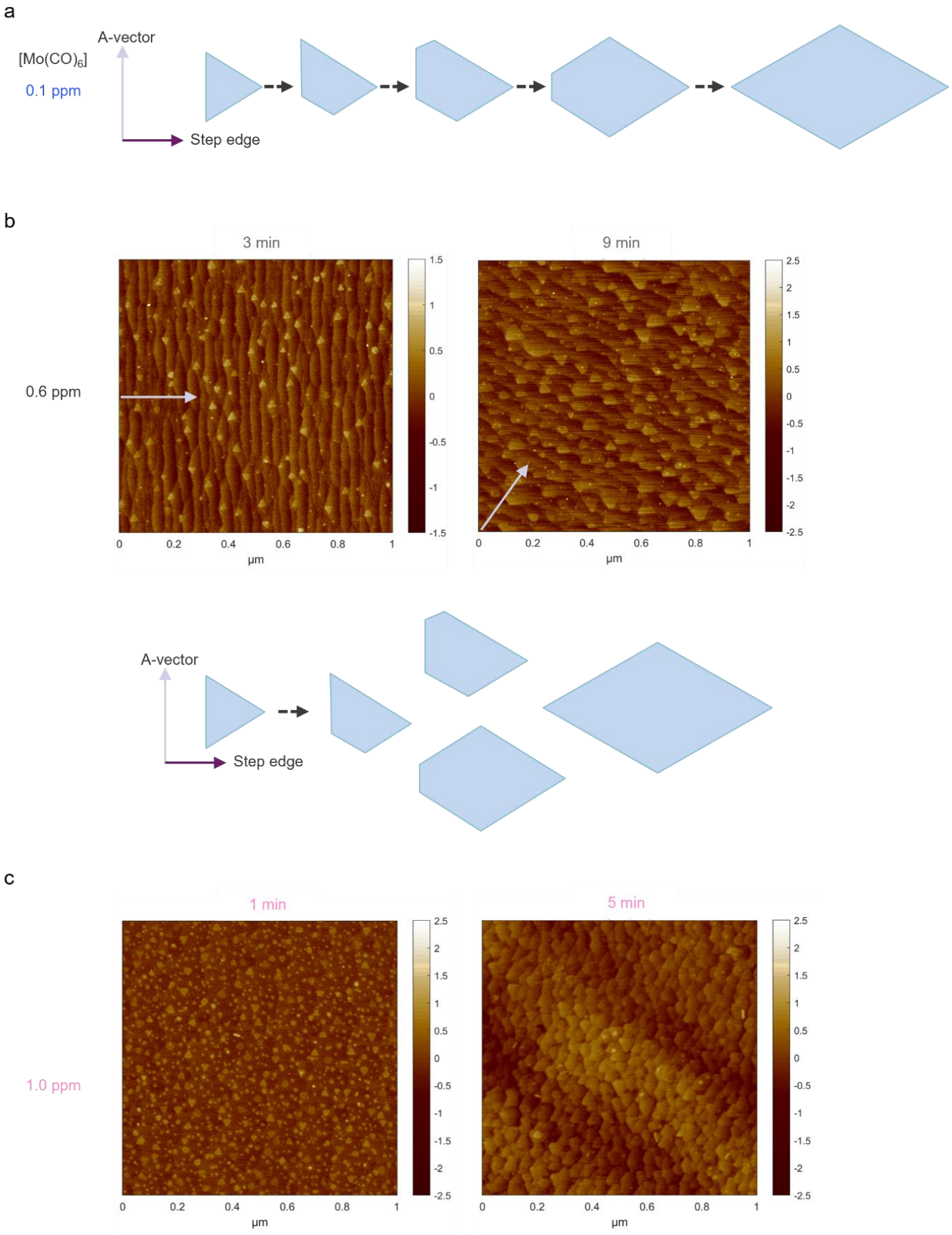

Figure S8. Schematic and AFM images of MoS_2 crystal shape evolution during MOCVD. The orientation of the A vector [11-20] is indicated by an arrow on the AFM images. **a**, Slow, step by step shape evolution at the lowest metal precursor concentration of 0.1 ppm. **b**, The different stages of crystal shape evolution coexist when the metal

precursor concentration is increased to 0.6 ppm. **c**, Crystal shape does not change at the higher metal precursor concentration of 1.0 ppm due to fast coalescence of the crystals.

Note 5. Recrystallization in multi-domain growth regime

The reduction of misoriented domains is a critical factor for optimizing performance and expanding the practical applications of 2D TMDs. The described van der Waals recrystallization process is highly beneficial to improve the crystallinity of the deposited MoS_2 monolayers, however, the energy required to recrystallize the misoriented domains depends on the structure of the formed grain boundaries. Following our experimental observations, effective 60° to 0° domains recrystallization during post deposition annealing (PDA) is possible in the MoS_2 monolayers, where the area of the 60° domains is below ≈ 20% upon the coalescence and the number of misoriented domains is below 1%. The β and γ grain boundary between the twin domains can be eliminated by one Mo or two S planes gliding, whereas a more complex mechanism is required to restore the high angle grain boundaries formed by the intermediate misoriented orientation towards the 0° orientation. In the case of the MoS_2 domains with the intermediate orientations, higher energy might be required to initiate the van der Waals recrystallization process, similar to the 3D materials recrystallization.[6] As a result, MoS_2 monolayers with the higher content of the misoriented domains (deposited with 1.0 and 1.3 ppm of Mo $(CO)_6$) do not recrystallize completely to the single-crystalline monolayer after 10 minutes recrystallization process (Figure 4a).

The extra energy for the van der Waals recrystallization of the intermediate oriented domains can be given by prolonged recrystallization time. Indeed, the misoriented domains coverage decreases from 40% to 15% when increasing the PDA time from 10 to 15 minutes (**Figure S9**). Moreover, the improved crystallinity of the MoS_2 monolayer after longer PDA is indicated by the sharpened GI-XRD peak along [11-20] direction(Figure S9d). The full width at half maximum (FWHM) of the peak decreases from 1.1 to 0.4 when the recrystallization time increases from 10 to 15 minutes, respectively. Furthermore, high-resolution scanning TEM (HR-STEM) confirms the presence of the remaining misoriented domains with the relative orientations of 15°, 20°, and 35° after 10 and 15 minutes of the PDA (Figure S9e, f, respectively). Thus, minimizing the number of misoriented domains before the layer coalescence is crucial to promote effective van der Waals recrystallization of those domains and to enable the self-oriented growth regime.

When optical spectroscopy is employed, the room temperature photoluminescence (RT-PL) response of MoS_2 monolayer grown in multi-domain regime shows significant differences between measurements taken under vacuum and those taken under non-vacuum conditions (**Figure S17**b). This suggests that the

removal of physisorbed species from the numerous defect sites reduces the excitonic responses under vacuum. Additionally, the defectivity of multi-domain MoS_2 was analyzed using three shorter recrystallization times (5-15 minutes) to assess the impact associated with the reduction of grain boundaries. This effect was also observed in the GI-XRD and DF-TEM responses (Figure S9c, d). A drastic improvement was noted in the ratio of integrated excitonic responses (I_{XD} *vs* I_{XA}) in cryogenic PL measurements when the recrystallization time was increased from 5 to 15 minutes (**Figure S10**a). The extracted defectivity index decreased from 9.4 to 5.8, and ultimately to 0.8, for the intervals of 5, 10, and 15 minutes of recrystallization processing time, respectively (Figure S10b). This improvement in the optical defectivity may be attributed to the reduced density of grain boundaries in the material after the recrystallization process. Despite the drastic improvement in the crystallinity of MoS_2 with the increasing recrystallization time, Raman derived strain/charge doping map demonstrates the slight change of the stain and the charge doping of the monolayer, similar to the single-crystalline MoS_2. This result indicates the role of the sapphire template/MoS_2 interaction on the Raman spectra.

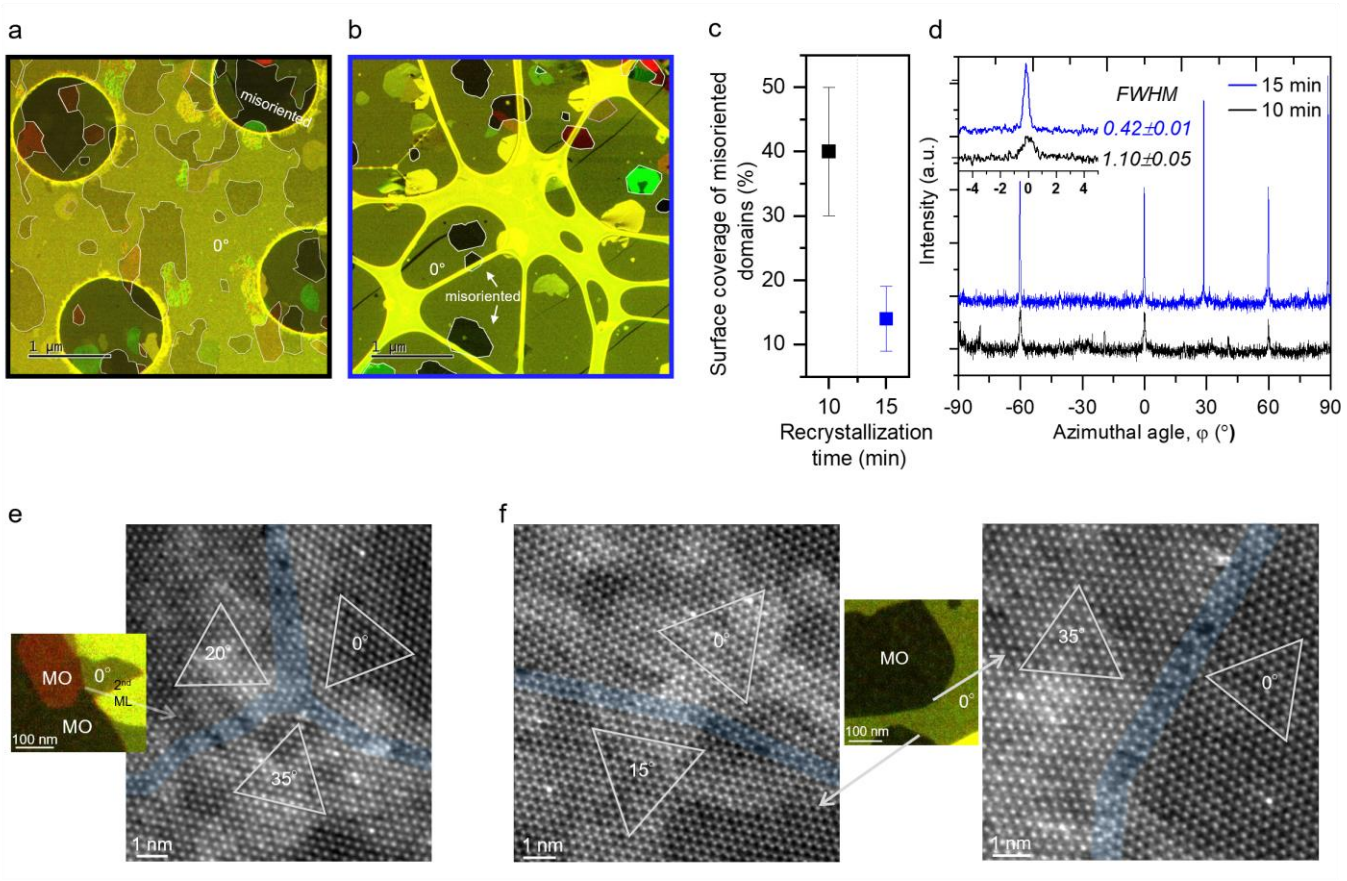

Figure S9. a, b, TEM images with false colors demonstrate the positive effect of prolonged PDA when the MoS_2 monolayer has a high number of misoriented domains. In the MoS_2 monolayer deposited with 1.0 ppm of $Mo(CO)_6$, after 10 minutes PDA, around 40% of the first monolayer consists of the misoriented (60° and intermediate) domains. **c,** The surface coverage of the misoriented domains decreases to 10% when PDA time increases from 10 to 15 minutes. **e, f,** HR-STEM images highlight the boundary area between the misoriented domains with relative 15°, 20°,

and 35° rotation after 10 (e) and 15 (f) minutes of recrystallization. The composite TEM image shows the large field of view of the inspected areas.

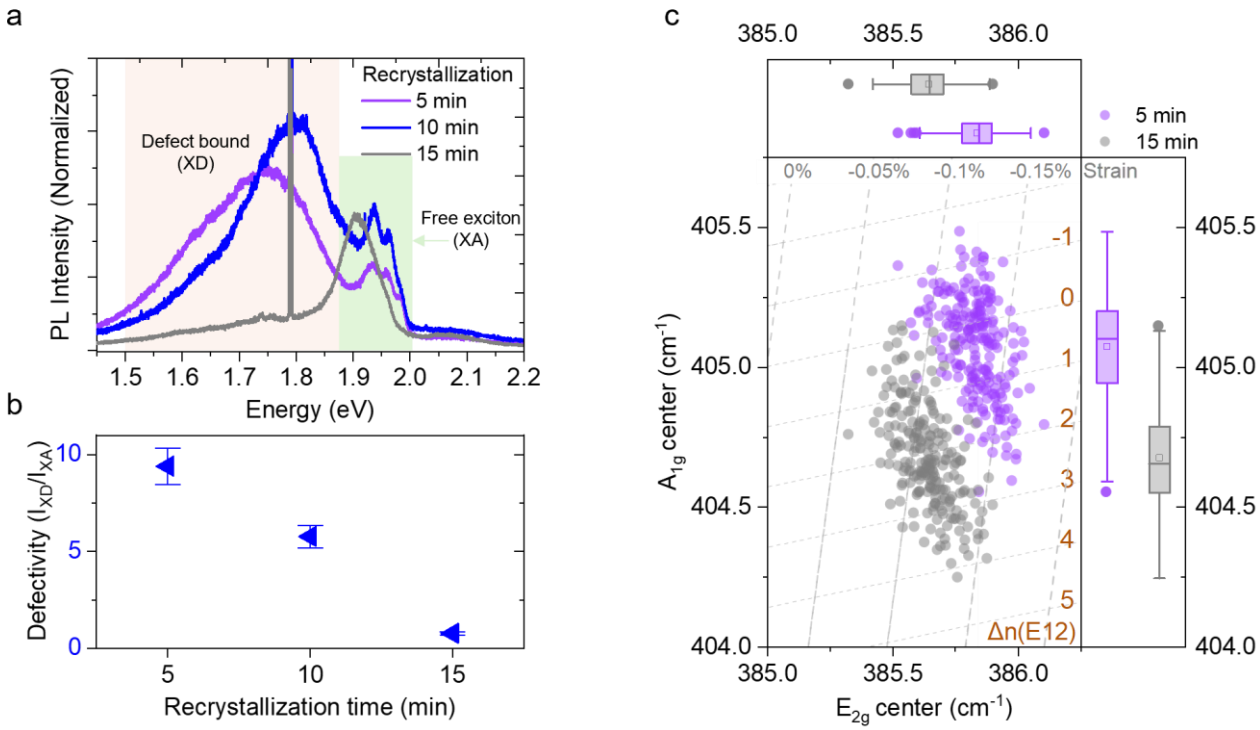

Figure S10. Improved crystallinity with recrystallization time influences the optical response of MoS_2 monolayers growth in multidomain growth regime. **a**, Cryogenic PL at 78K demonstrate the notable spectra change for multi-domain MoS_2 monolayers with the recrystallization time. The deconvoluted spectra are presented in Figure S18. **b**, This is reflected in the extracted defectivity index (I_{XD} to I_{XA}), as a ratio of integral intensity of defect-bound to free excitons. c, Mapping A_{1g} and E_{2g} phonon peaks extracted from Raman spectra is used to assess strain and relative change in doping of MoS_2 monolayer during recrystallization. MoS_2 monolayers are deposited using 1.0 ppm of $Mo(CO)_6$.

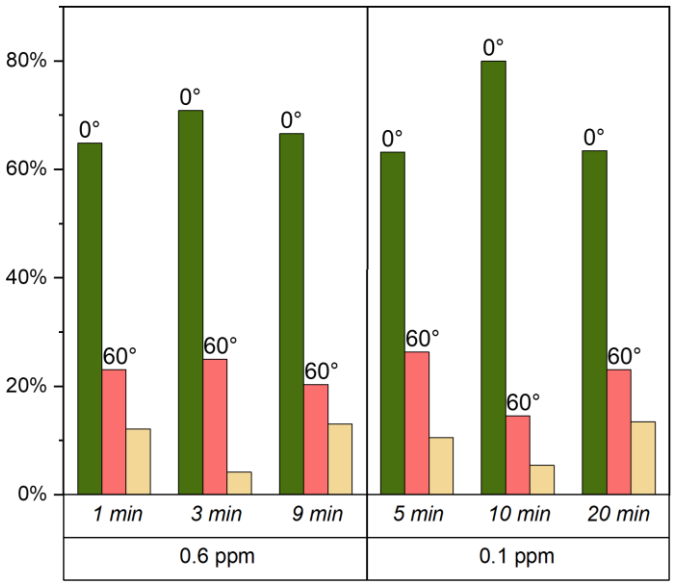

Figure S11. Percentage of 0° and 60° oriented crystals (green and red, respectively) during the different growth stages of MoS_2 crystals deposited with 0.6 and 0.1 ppm. The misoriented crystals are indicated in orange.

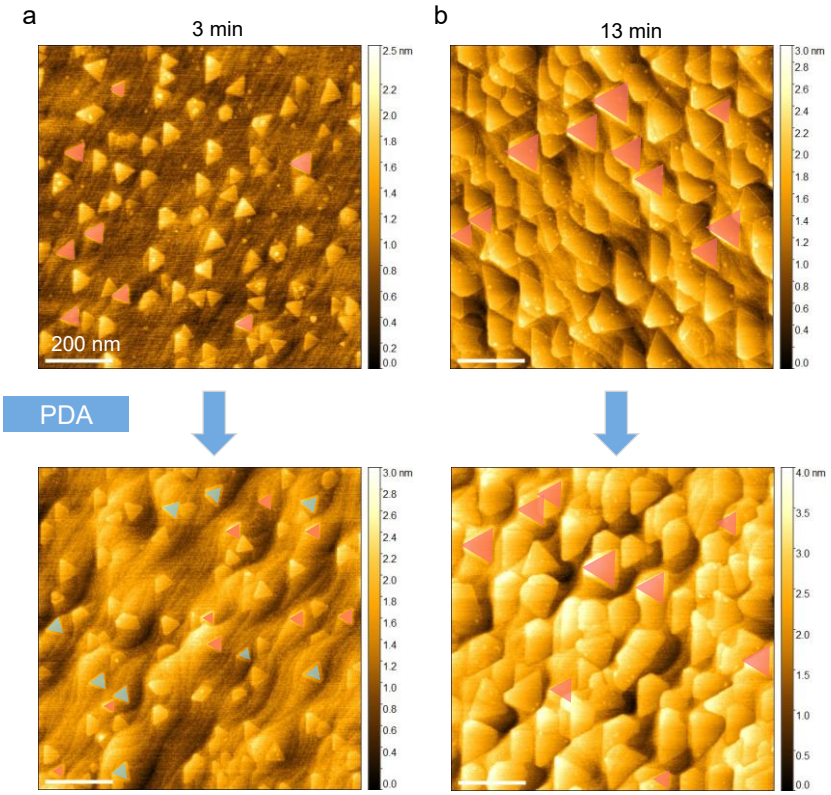

Figure S12. Effect of 10 min of post-deposition annealing (PDA) in H_2S on the orientation of the isolated MoS_2 crystals deposited with 0.6 ppm of $Mo(CO)_6$. Some 60° oriented crystals are highlighted in red. Transition 60° to 0° orientation is not observed. PDA causes more pronounced surface reconstruction and leads to an increase of the number of misoriented domains (in blue).

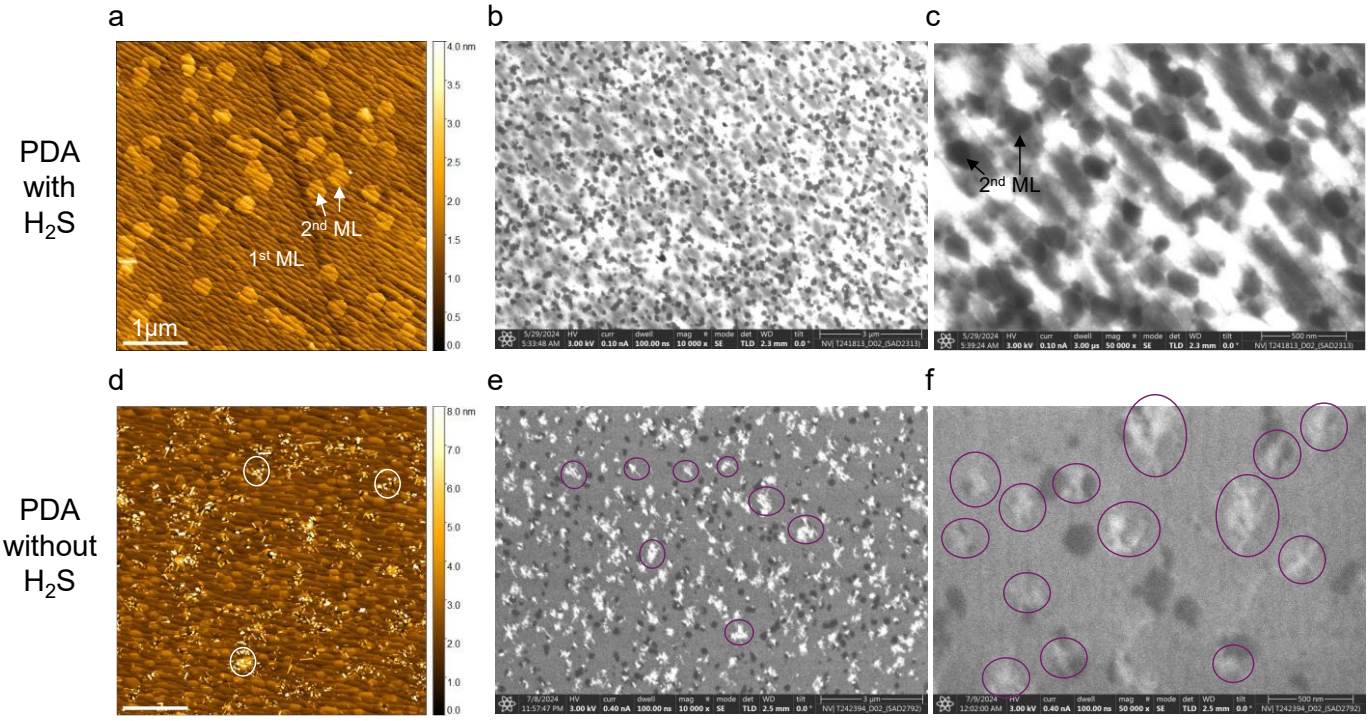

Figure S13. Effect of the atmosphere during 10 minutes of PDA at 1000 °C on the morphology of the closed MoS_2 monolayer deposited with 0.6 ppm of $Mo(CO)_6$. PDA without H_2S damages the first monolayer as well as the bilayer islands (indicated by the black arrows). The contrast in the SEM images of the closed MoS_2 monolayer is attributed to the water intercalation (b, c).

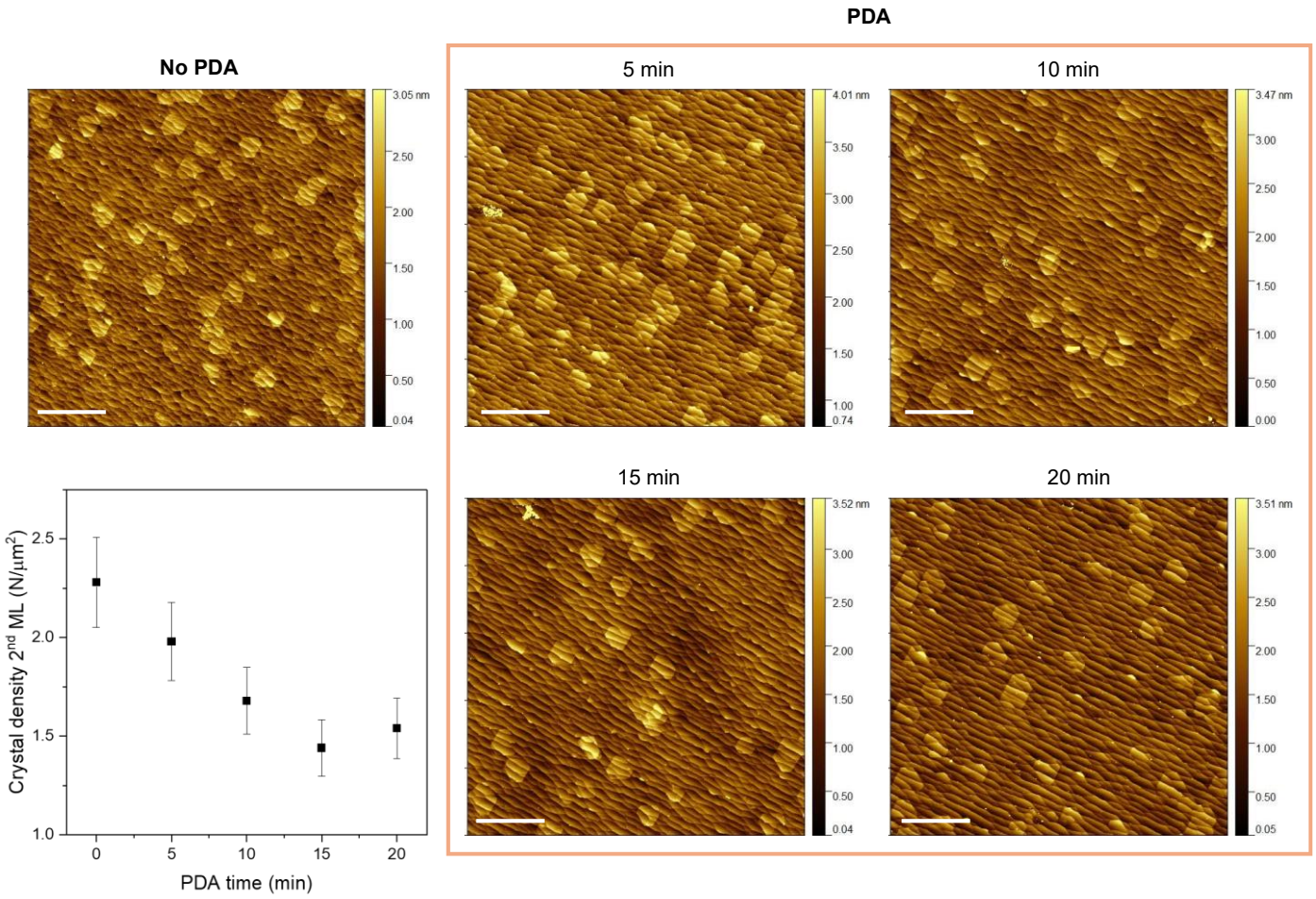

Figure S14. Decreasing 2nd MoS_2 monolayer crystal density with increasing PDA time. The MoS_2 monolayers are deposited with 0.6 ppm of $Mo(CO)_6$, and PDA is performed in H_2S at 1000 °C.

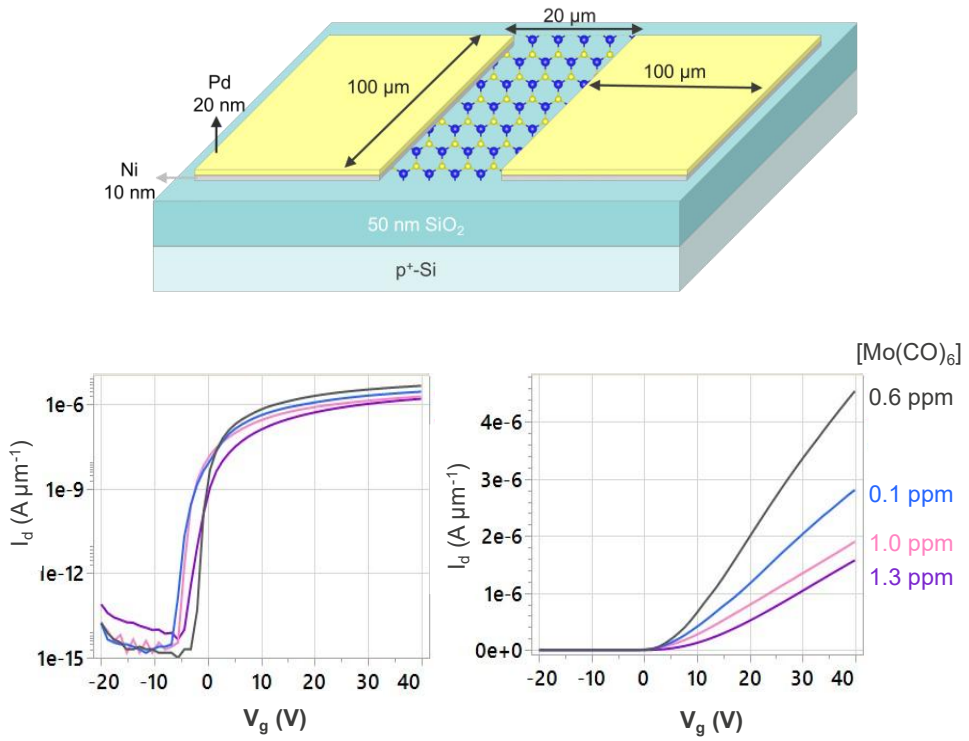

Figure S15. A schematic of the back-gated FET and drain current for MoS_2 monolayers presented in Figure 4c (top). The recrystallization time of 10 min is applied to all MoS_2 monolayers after a layer closure. A higher drain current (I_d) is observed for the lower metal precursor concentrations of 0.6 ppm and 0.1 ppm. A linear (right) and a logarithmic (left) scale are depicted as a function of gate voltage (V_g) for 1V drain voltage.

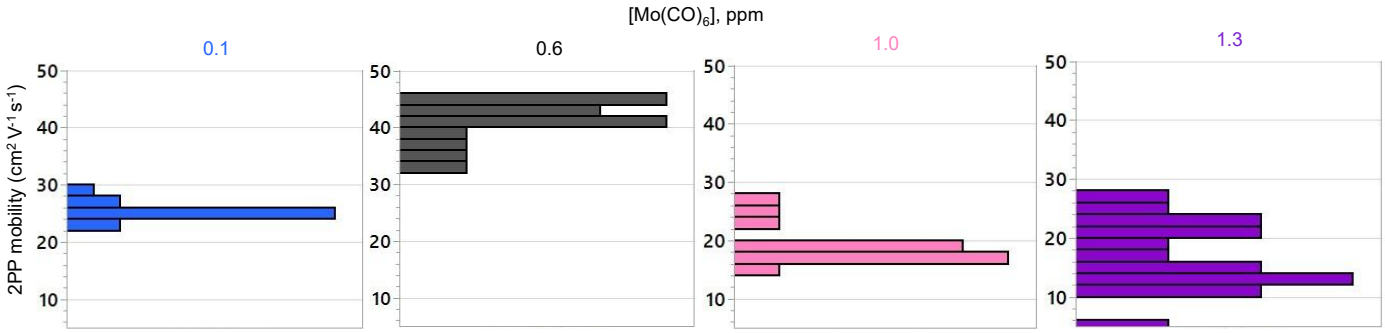

Figure S16. Statistical distribution of the 2pp mobility measured in the lab-fabricated back-gated FET with MoS_2 active layer.

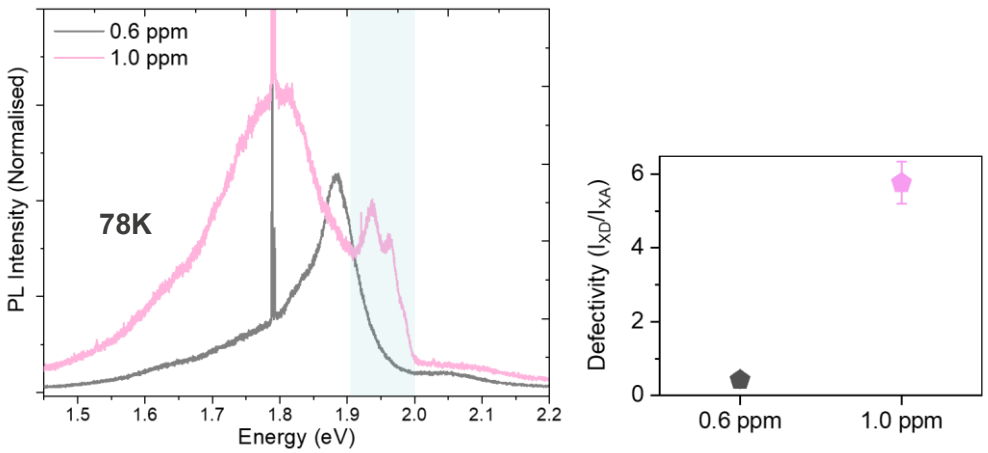

Figure S17. Cryogenic photoluminescence (PL) at 78K reveals a 98 meV shift (blue line) between singlecrystalline (0.6 ppm) MoS_2 monolayer and MoS_2 monolayer with misoriented domains (1.0 ppm) due to an impact of interface

charges. The defectivity index is extracted from cryogenic PL and is higher for the monolayers containing misoriented domains compared to single-crystalline MoS_2 monolayer.

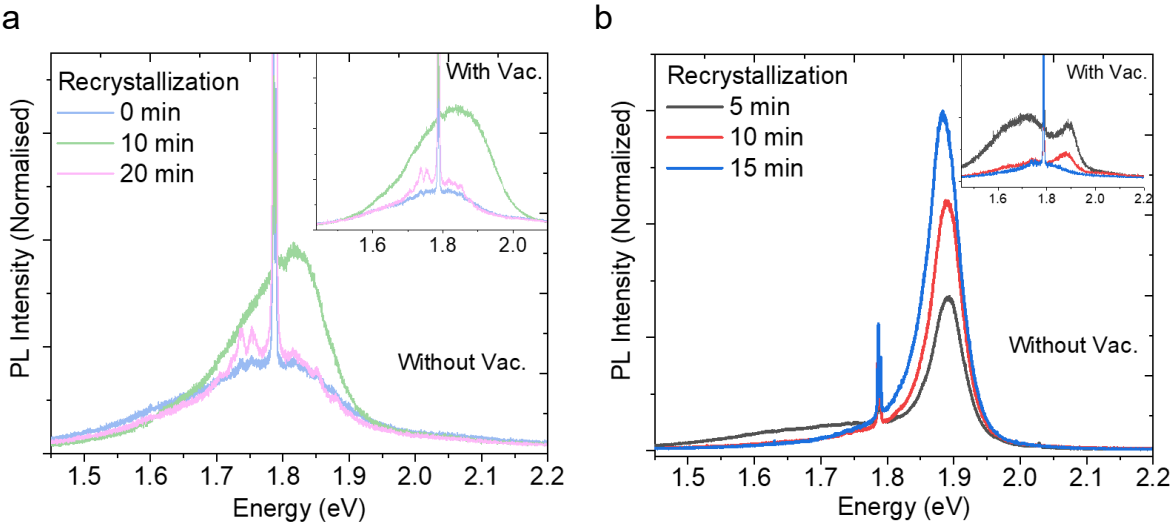

Figure S18. Room temperature photoluminescence (RT-PL) with and without vacuum for MoS_2 monolayers deposited with 0.6 (a) and 1.0 ppm (b) of $Mo(CO)_6$ after different recrystallization times. The room temperature responses tend to change significantly when transitioning from a non-vacuum to a vacuum environment. This is due to various atmospheric species, such as O_2, H_2O, and organic molecules, which can physisorb onto the defective surfaces (including grain boundaries) of monolayer MoS_2. **a**, Here, the negligible differences in RT-PL responses between the vacuum and non-vacuum conditions confirm the high quality and lower presence of defect centers in the single-crystalline MoS_2 monolayer grown in self-oriented growth regime. **b**, This is in contrast with MoS_2 monolayers grown in multi-domain regime, where a pronounce difference in RT-PL is observed between vacuum and non-vacuum conditions.

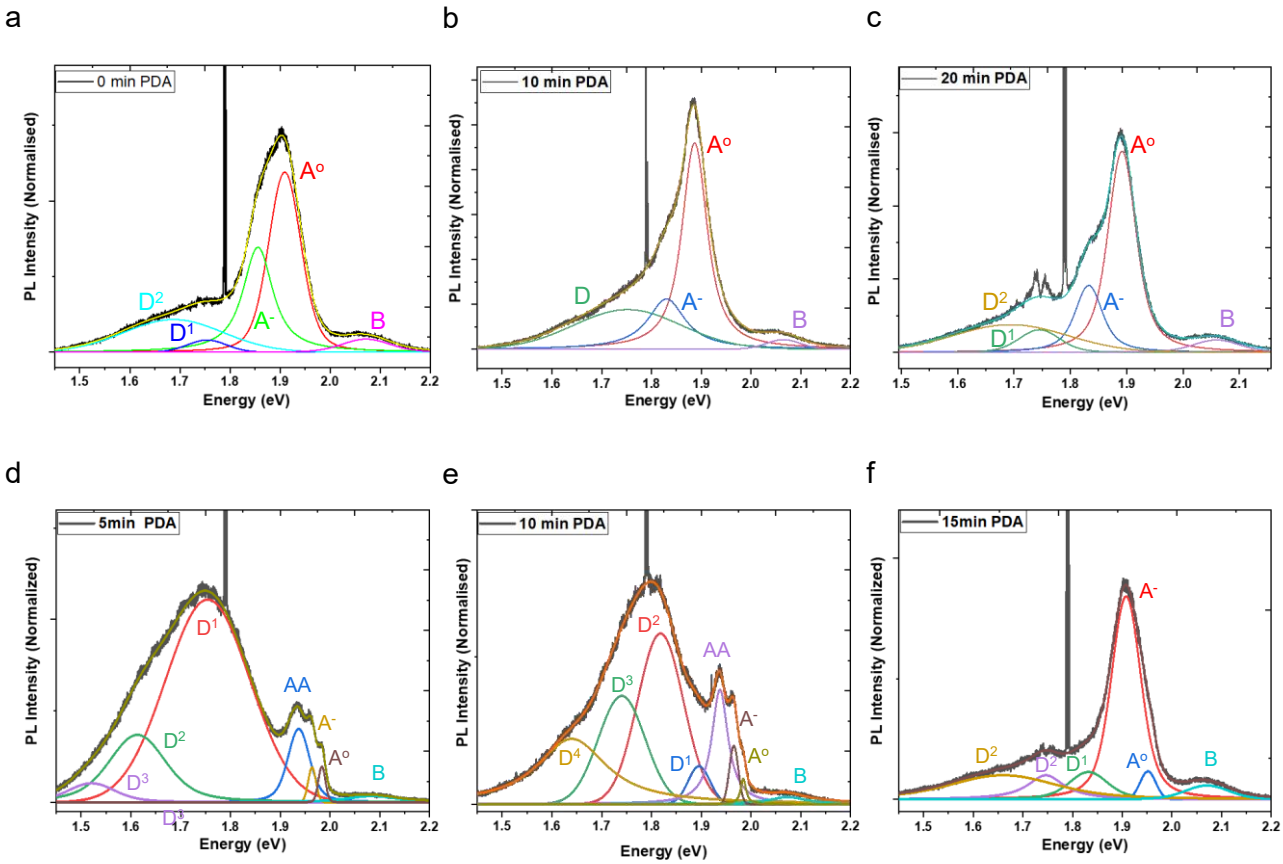

Figure S19. Deconvolution of the cryogenic PL at 78K from Figure 5a and -d after different recrystallization times using the Lorentzian function. MoS_2 monolayers were deposited with 0.6 (a, b, c) and 1.0 ppm (d, e, f) of $Mo(CO)_6$. The spectra in (a, b, c) and (d, e, f) correspond to Figure 5a and -d, respectively. A^o, A^-, AA, B, and D correspond to neutral exciton, charged exciton (trion), biexciton, B exciton, and low temperature defect bands, respectively. If the fitting results in the few defect bands, they are numbered D^1, D^2, etc.

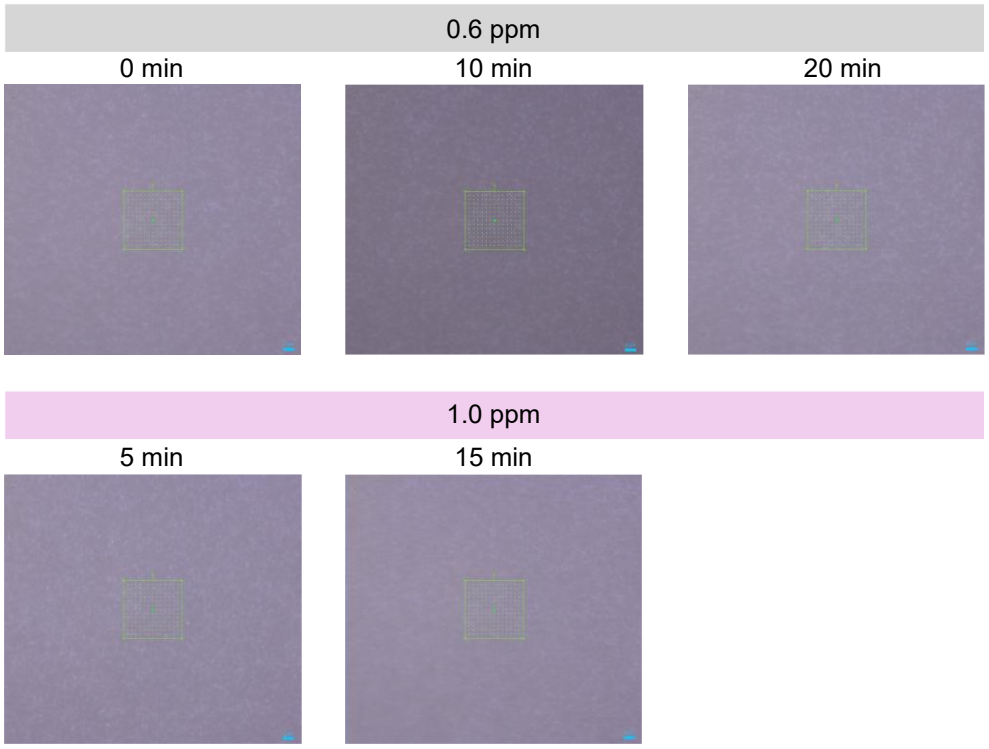

Figure S20. Optical images of the areas where 225 Raman spectra were acquired of MoS_2 monolayers on sapphire deposited with 0.6 and 1.0 ppm of $Mo(CO)_6$.

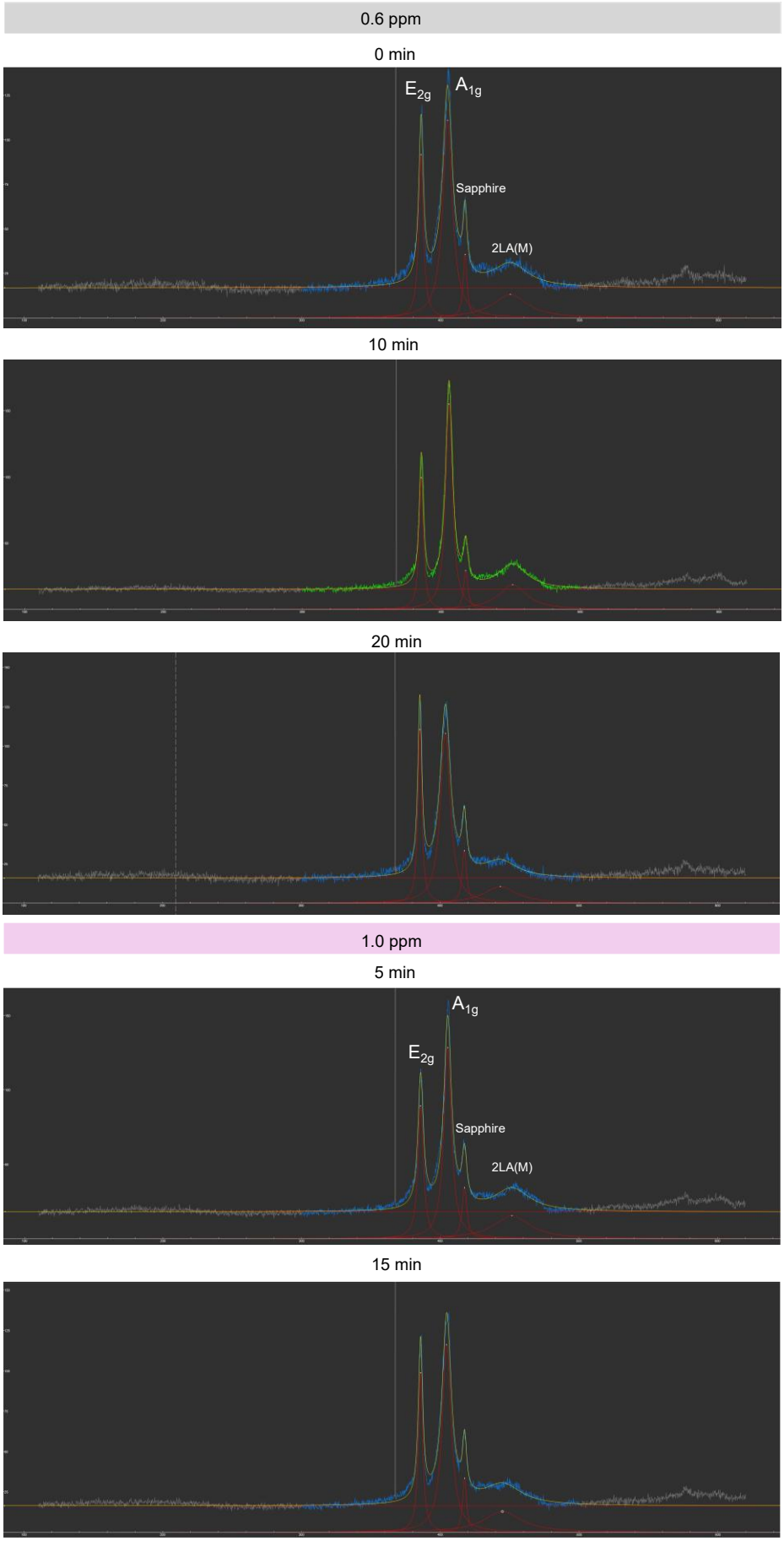

Figure S21. Typical Raman spectral response, obtained from MoS_2 monolayer deposited with 0.6 and 1.0 ppm of $Mo(CO)_6$ after different recrystallization times.

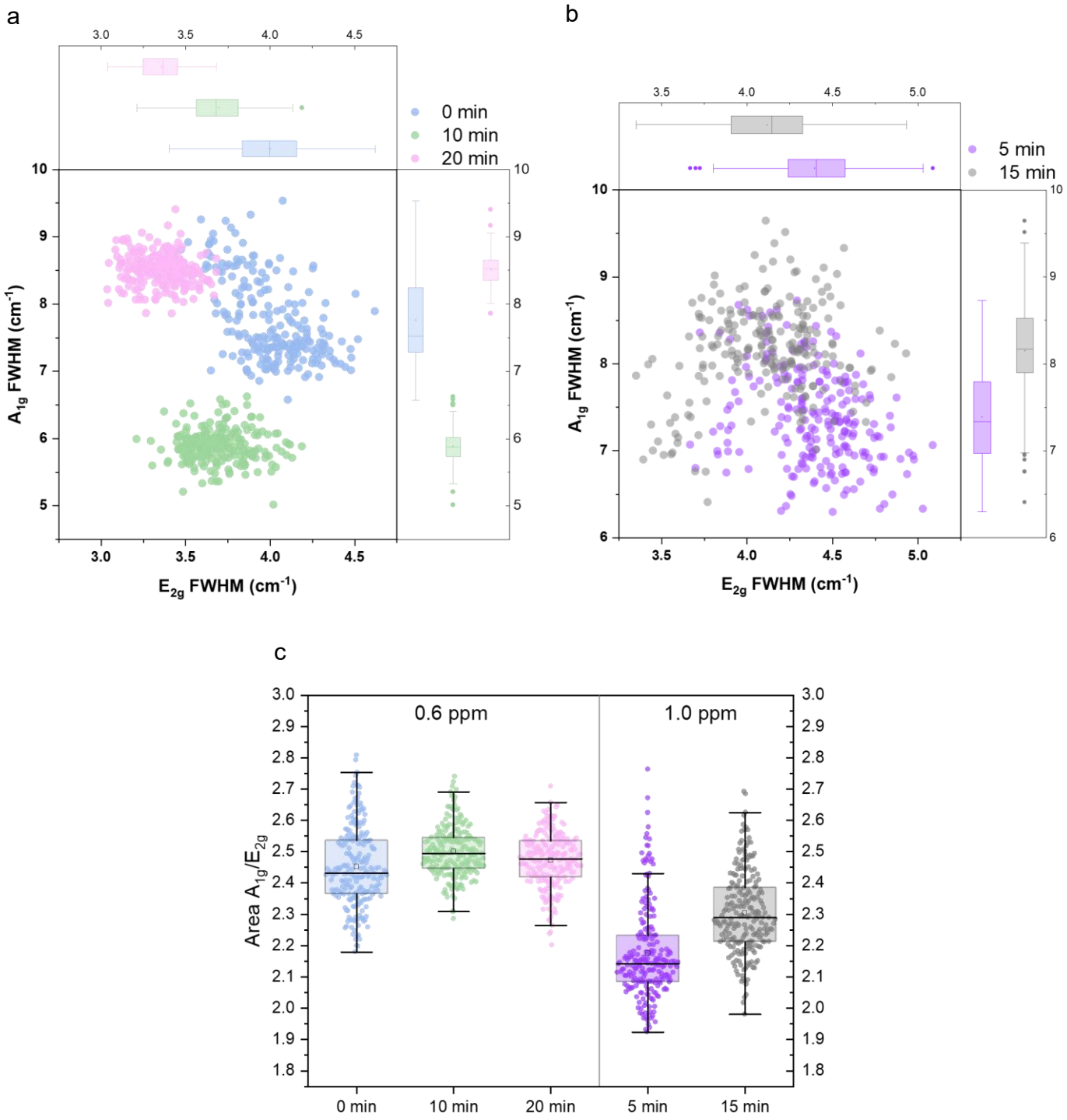

Figure S22. Statistical interpretation of the extracted A_{1g} and E_{2g} peaks from Raman spectral response, obtained from MoS_2 monolayer deposited with 0.6 (a) and 1.0 ppm (b) of $Mo(CO)_6$ after different recrystallization times.

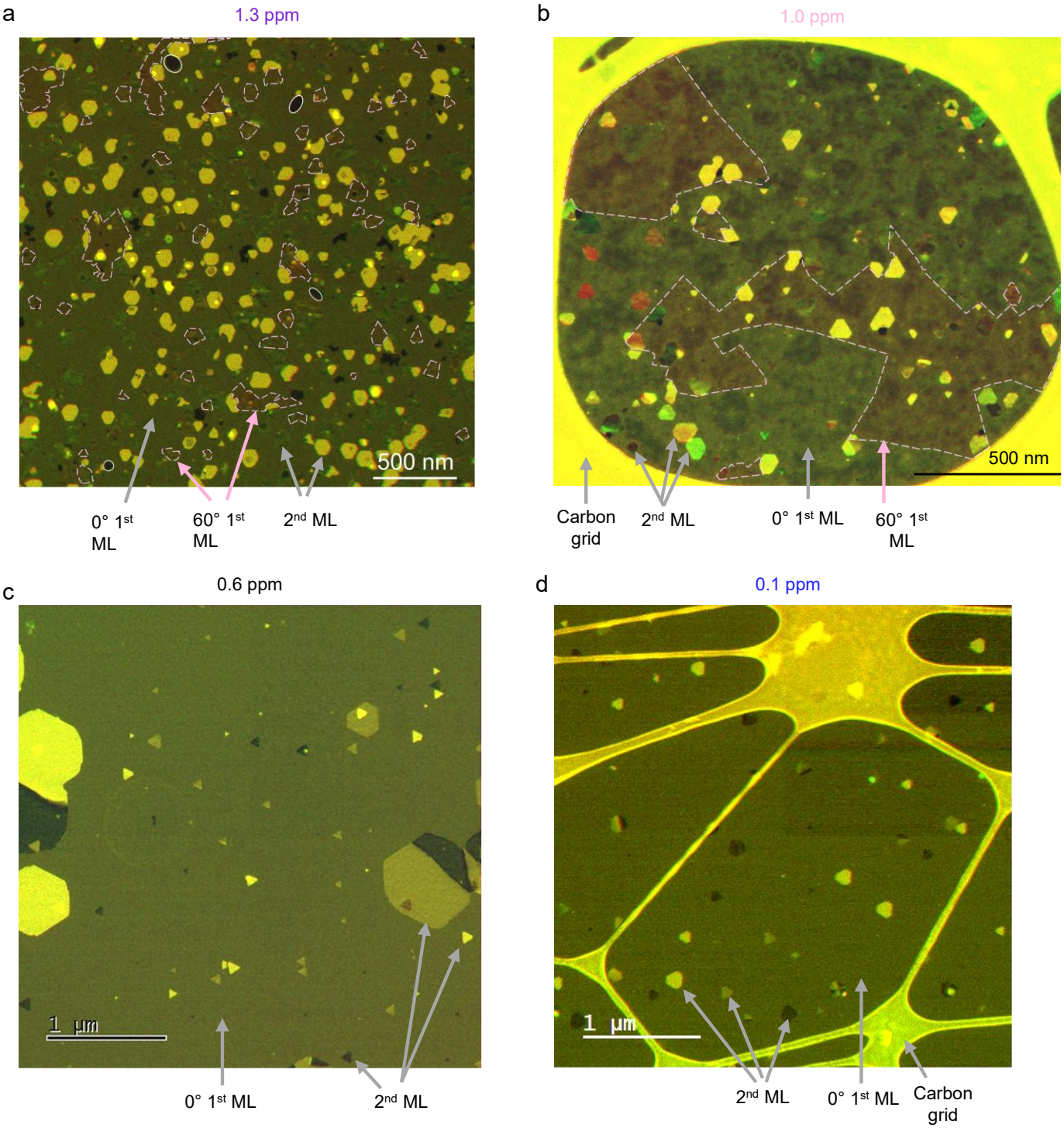

Figure 23. Large field of view composite TEM images of MoS_2 monolayers presented in Figure 4a.

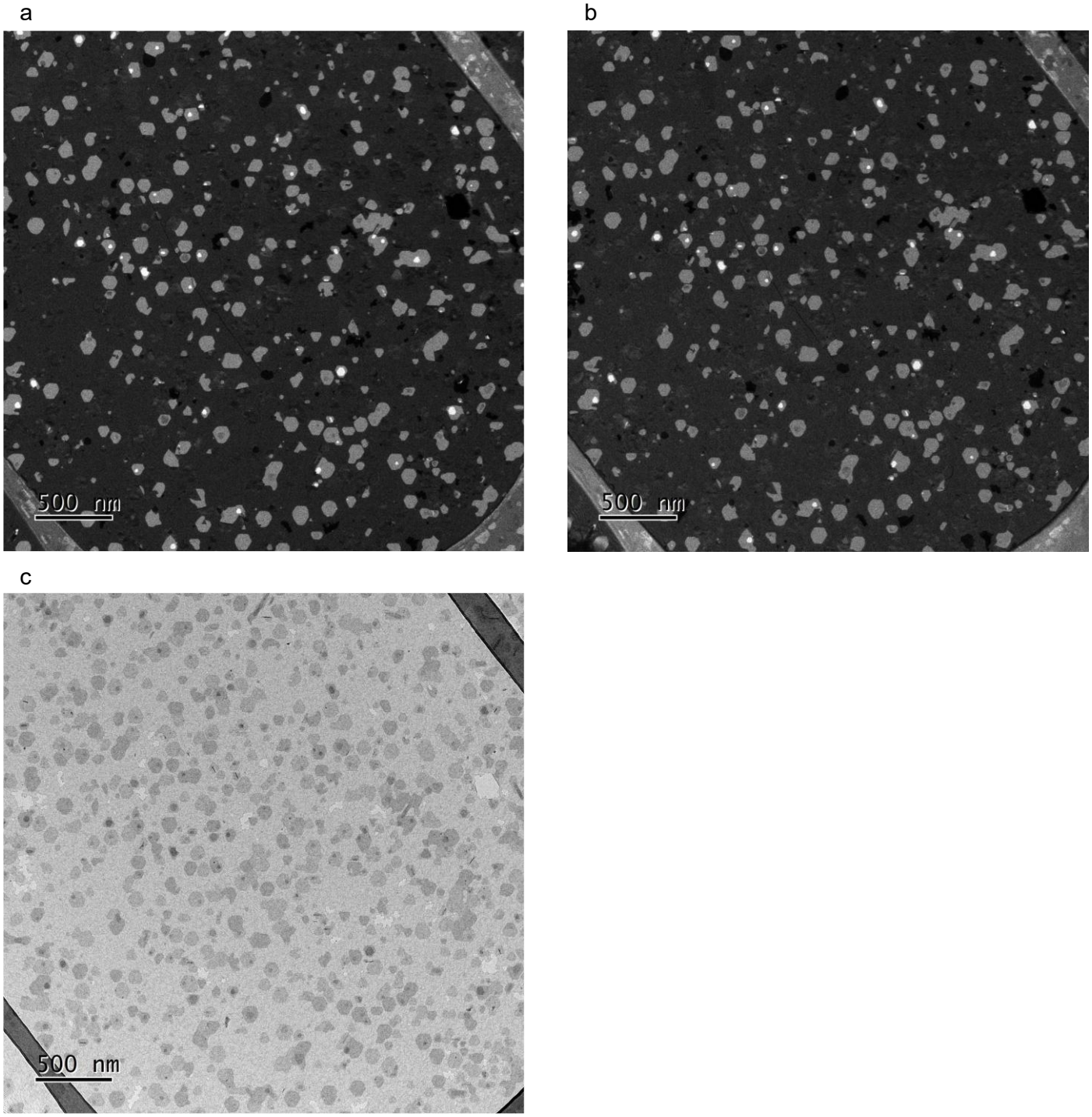

271

272 **Figure S24.** The dark-field TEM images (a, b) of the MoS_2 monolayer used for the composite image with false colors
273 in Figure S23a. A bright-field TEM image of the same area is presented in (c).

274

275

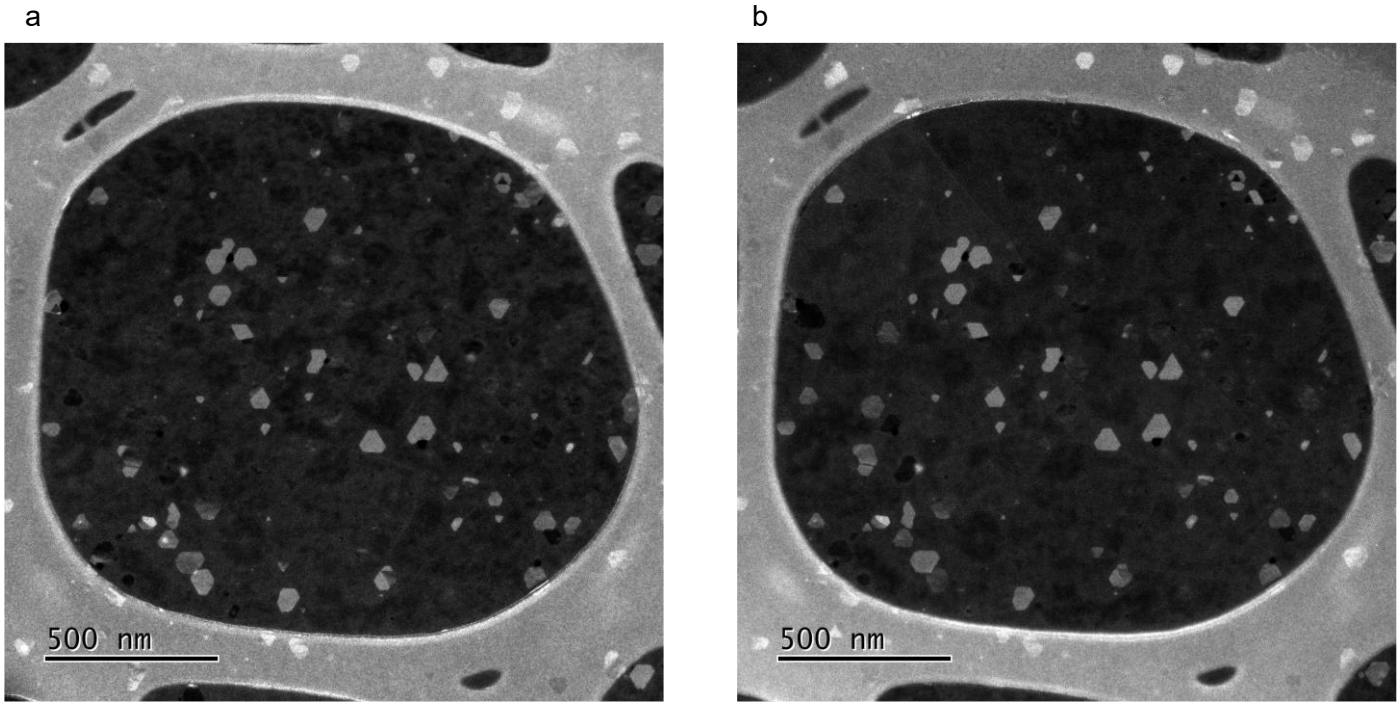

Figure S25. The dark-field TEM images (a, b) of the MoS_2 monolayer used for the composite image with false colors in Figure S23b.

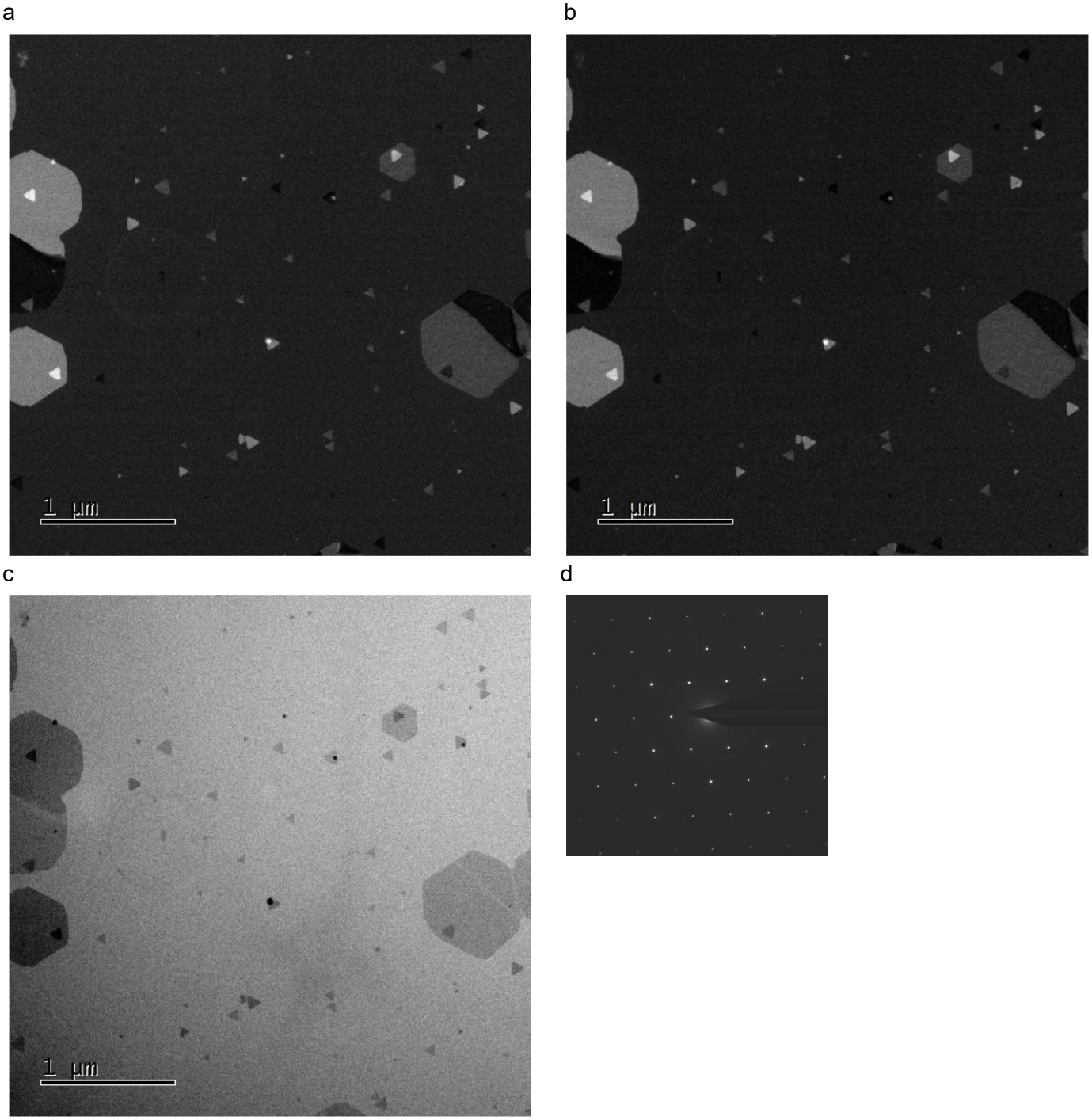

Figure S26. The dark-field TEM images (a, b) of the MoS_2 monolayer used for the composite image with false colors in Figure S23c. A bright-field TEM image and a diffraction pattern of the same area is presented in (c) and (d), respectively.

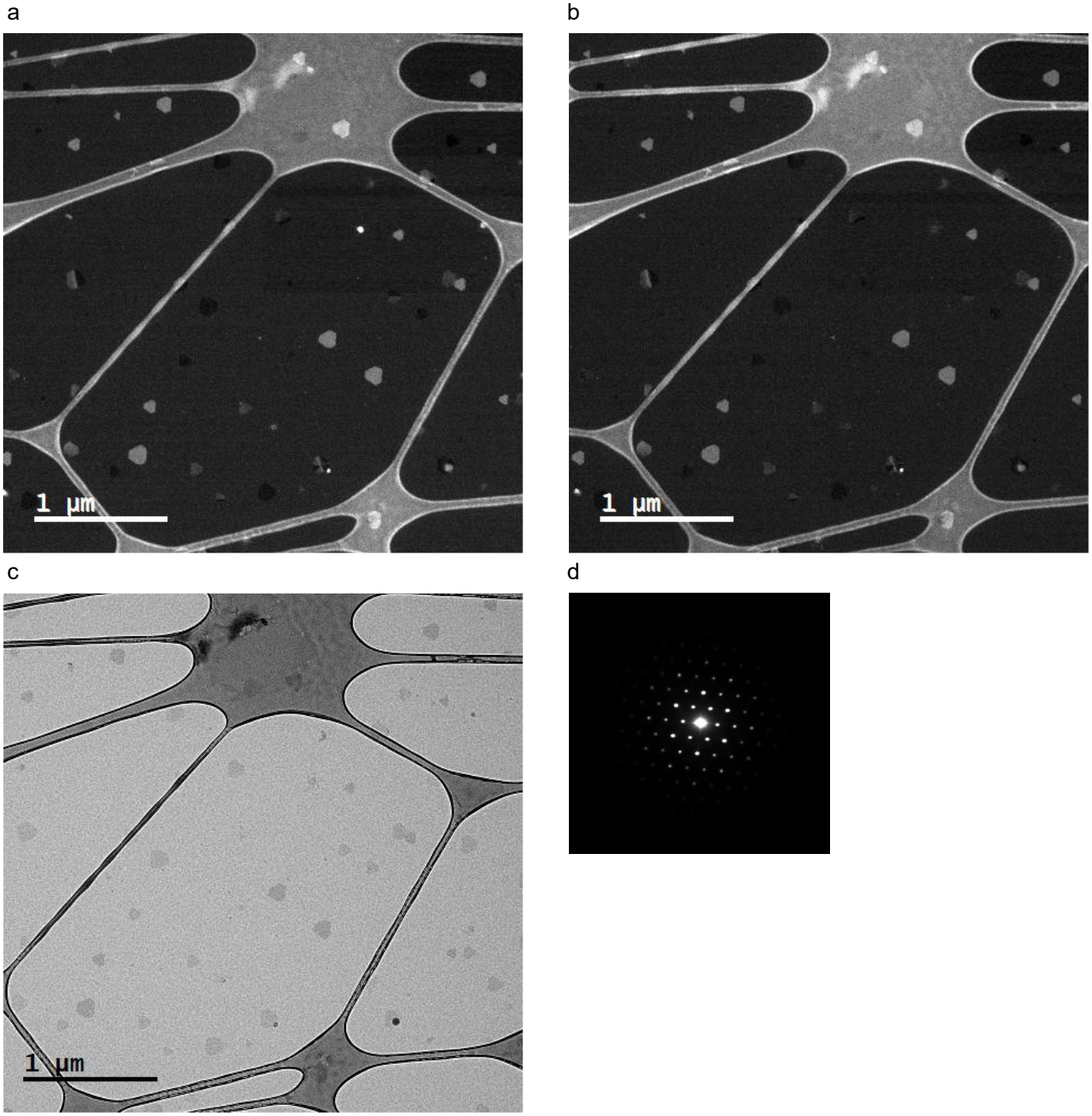

Figure S27. The dark-field TEM images (a, b) of the MoS_2 monolayer used for the composite image with false colors in Figure S23d. A bright-field TEM image and a diffraction pattern of the same area is presented in (c) and (d), respectively.

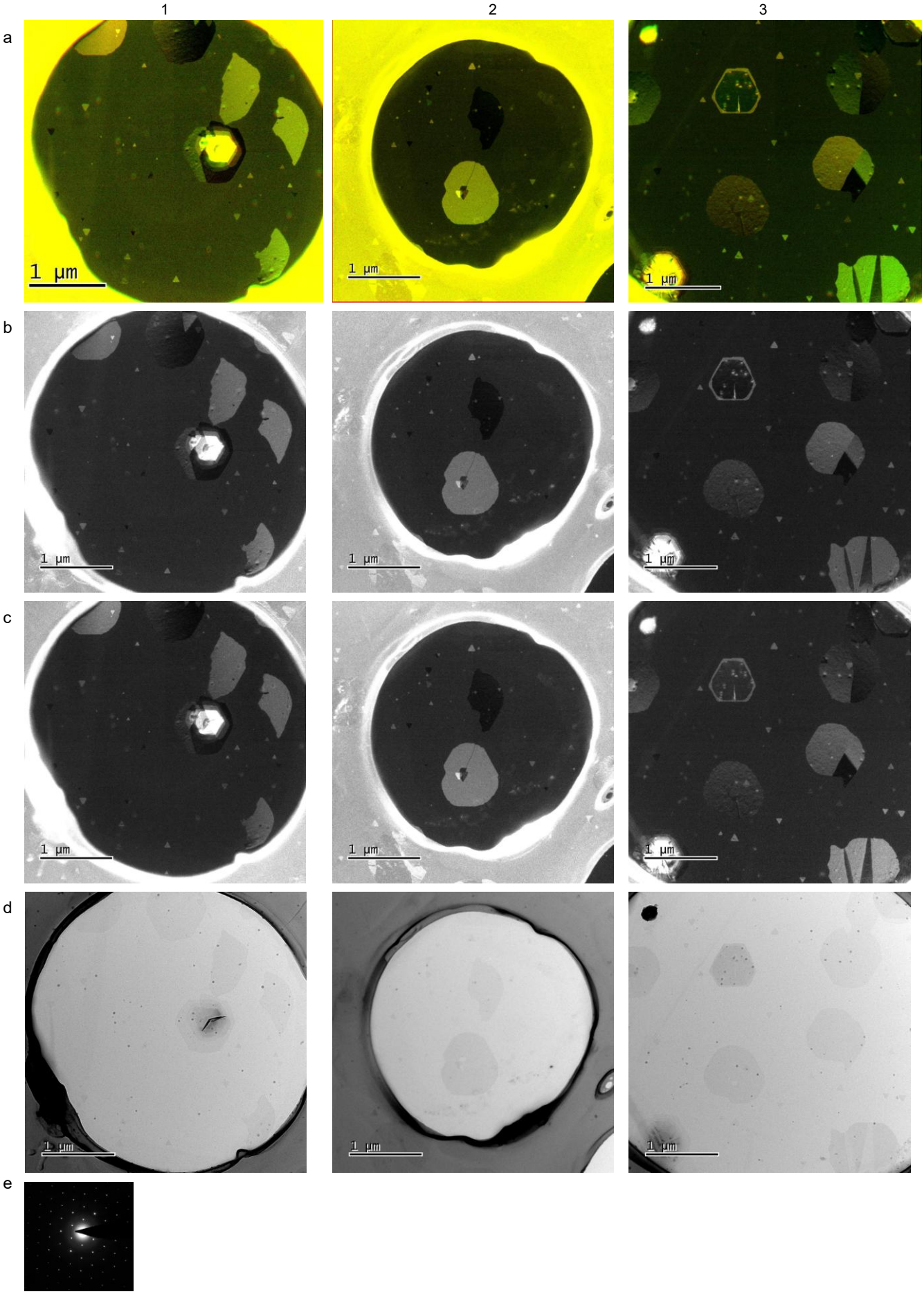

287

288 **Figure S28**. The additional TEM images from 3 regions for the MoS_2 monolayers deposited with 0.6 ppm of $Mo(CO)_6$,
289 demonstrating the single-crystalline nature of the film. The composite images with false colors (a) are composed

using the dark-field TEM images (b, c). The bright-field TEM images and a diffraction pattern of the same area are presented in (d) and (e), respectively.

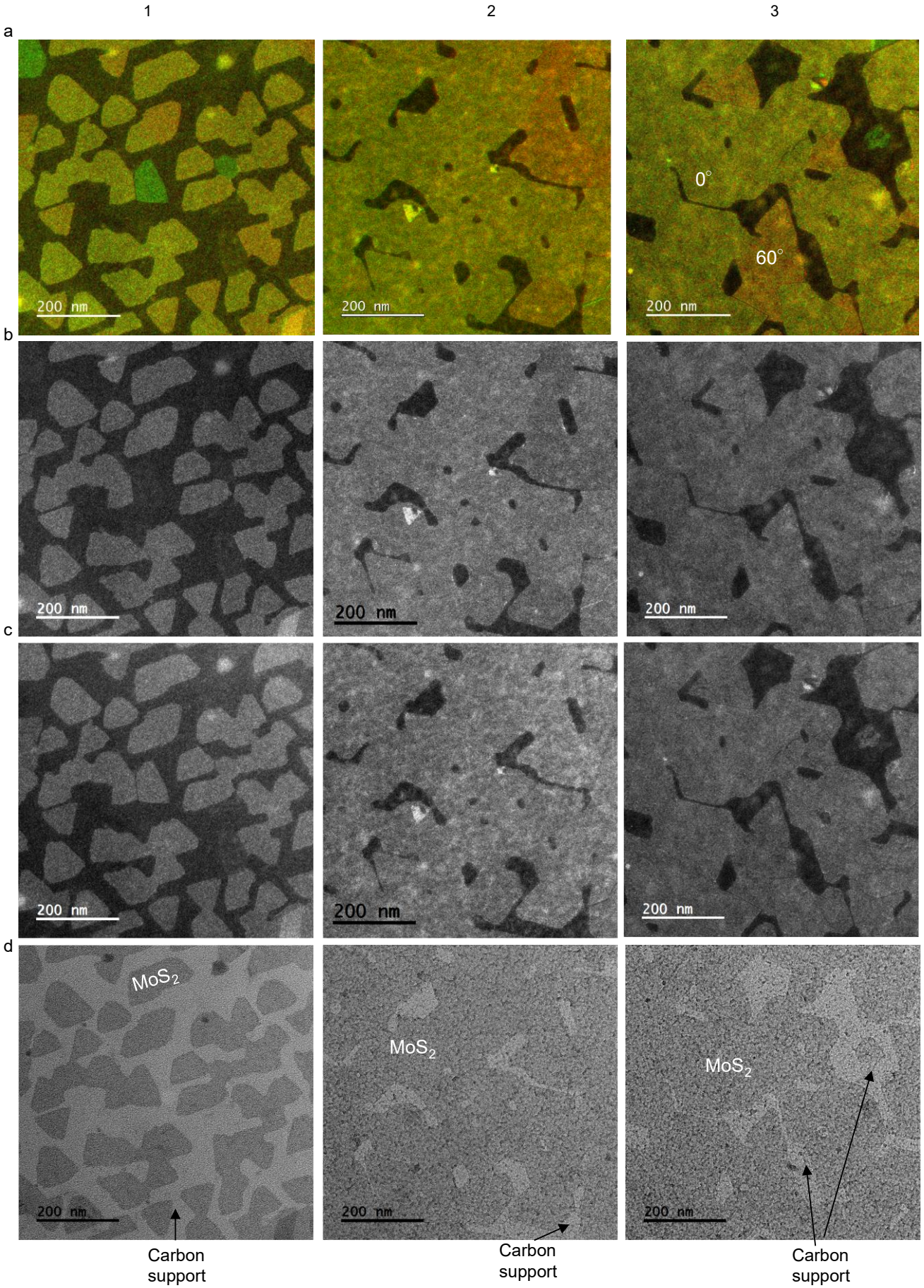

Figure S29. The TEM images from 3 of the MoS_2 crystals deposited with 0.6 ppm of $Mo(CO)_6$ for 13 min (1) and 19 min (2 and 3). The composite images with false colors (a) are composed using the dark-field TEM images (b, c). The bright-field TEM images are presented in (d). The composite images from regions 1 and 2 were used in Figure 2b.

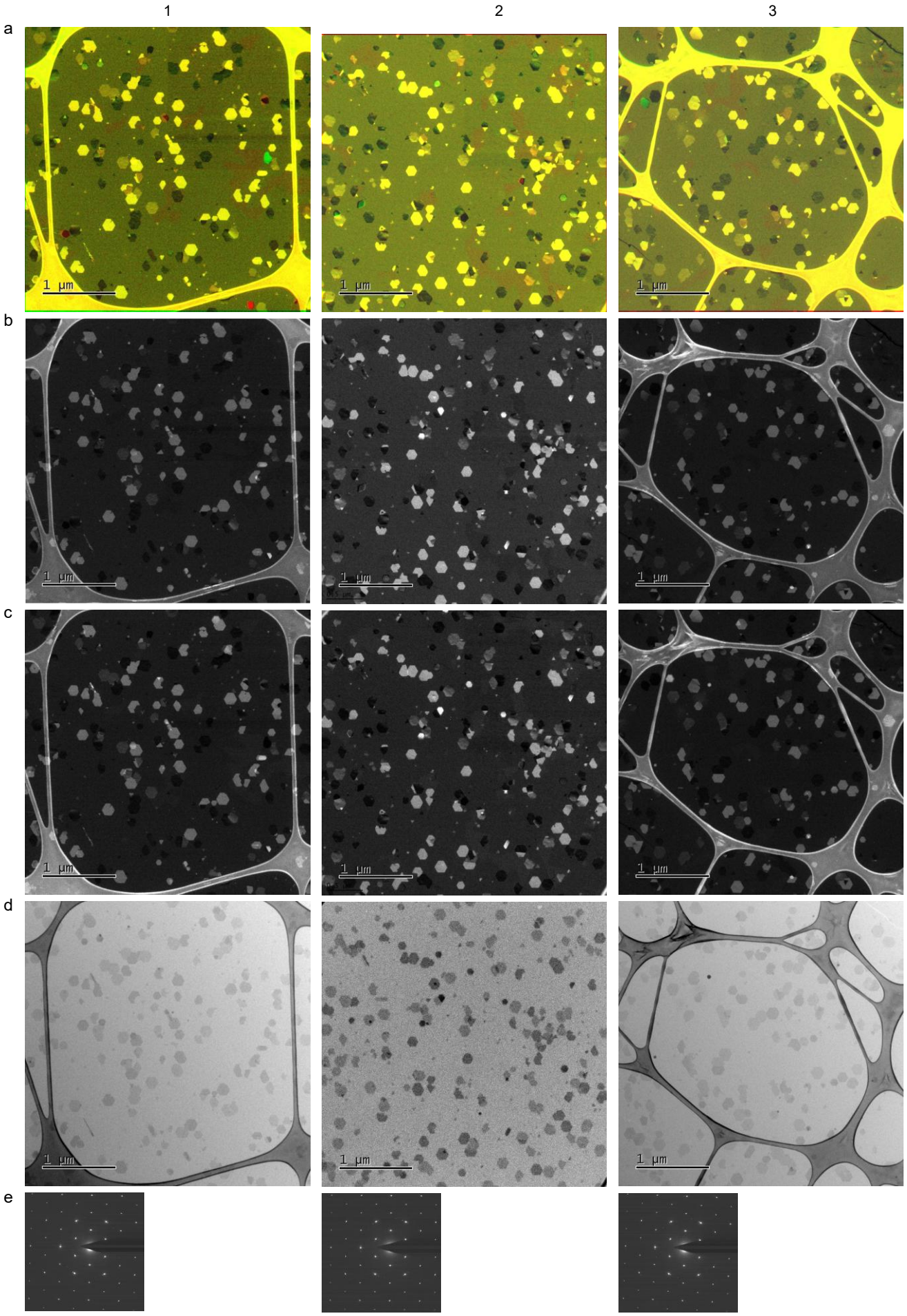

Figure S30. The TEM images from 3 regions for the MoS_2 monolayer deposited with 0.6 ppm of $Mo(CO)_6$ for 22 min (Sample 1). The composite images with false colors (a) are composed using the dark-field TEM images (b, c). The red

areas on the composite images correspond to twin domains. The bright-field TEM images and the diffraction patterns are presented in (d) and (e), respectively. The composite image from region 2 was used in Figure 2b.

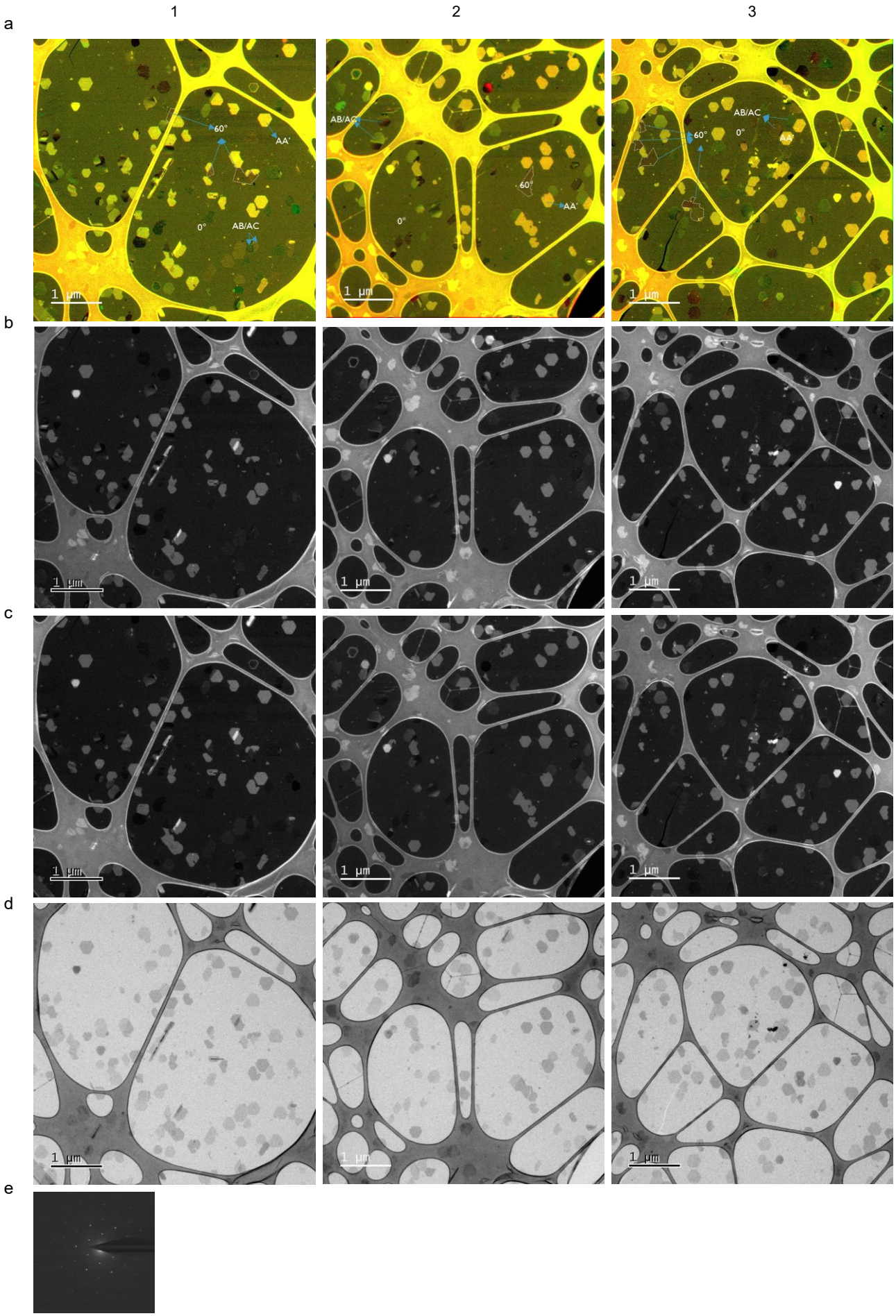

Figure S31. The TEM images from 3 regions for the MoS_2 monolayer deposited with 0.6 ppm of $Mo(CO)_6$ for 22 min (Sample 2). The composite images with false colors (a) are composed using the dark-field TEM images (b, c). The red

areas on the composite images correspond to twin domains, as highlighted on the images. The stacking of the second layer islands is also highlighted. The bright-field TEM images and a diffraction pattern are presented in (d) and (e), respectively.

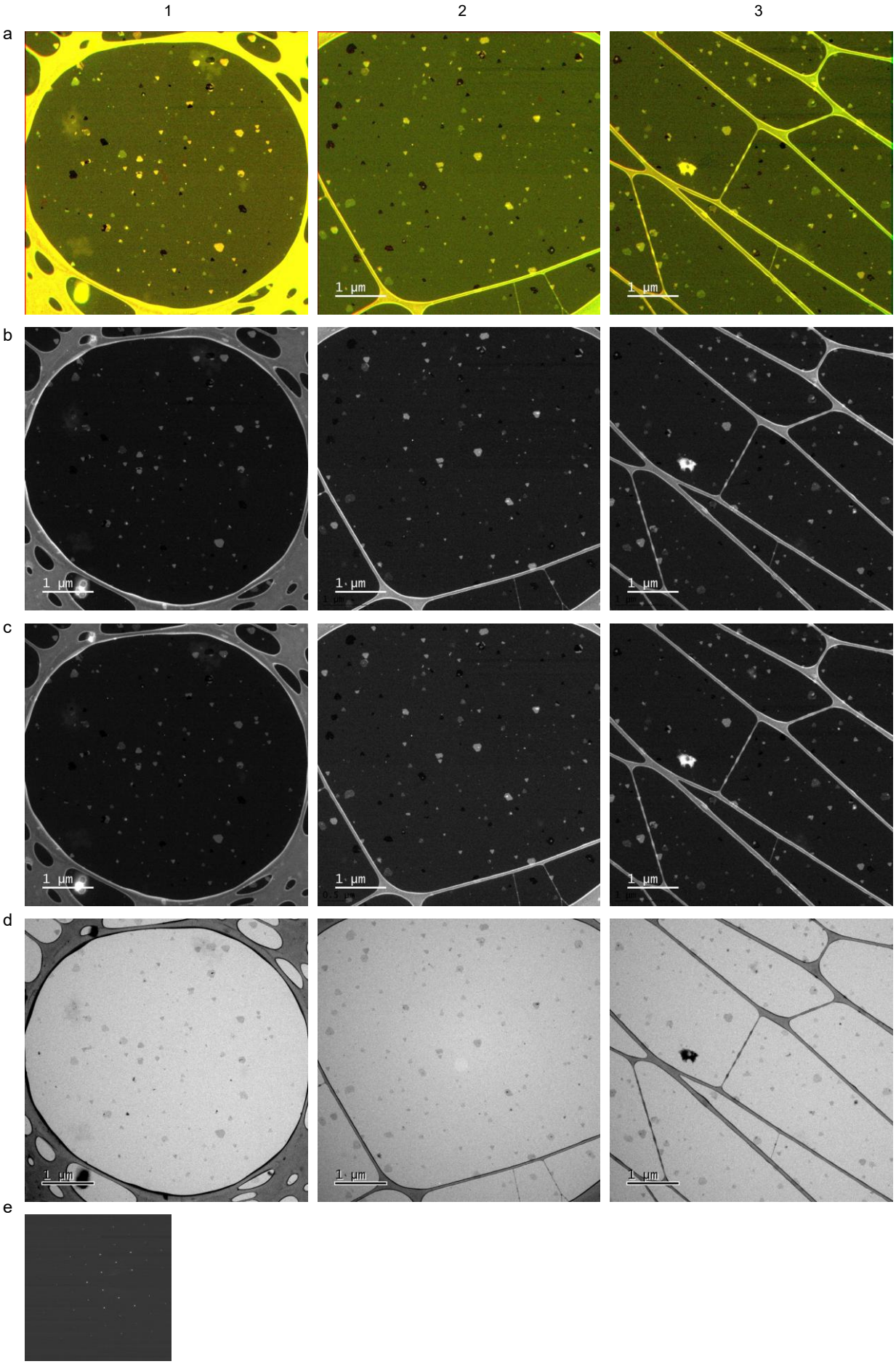

Figure S32. The TEM images from 3 regions for the MoS_2 monolayer deposited with 0.6 ppm of $Mo(CO)_6$ for 22 min, followed by 10 mins of the post-deposition annealing. The composite images with false colors (a) are composed using

the dark-field TEM images (b, c). The bright-field TEM images and a diffraction pattern are presented in (d) and (e), respectively. The composite image from region 2 was used in Figure 2b.

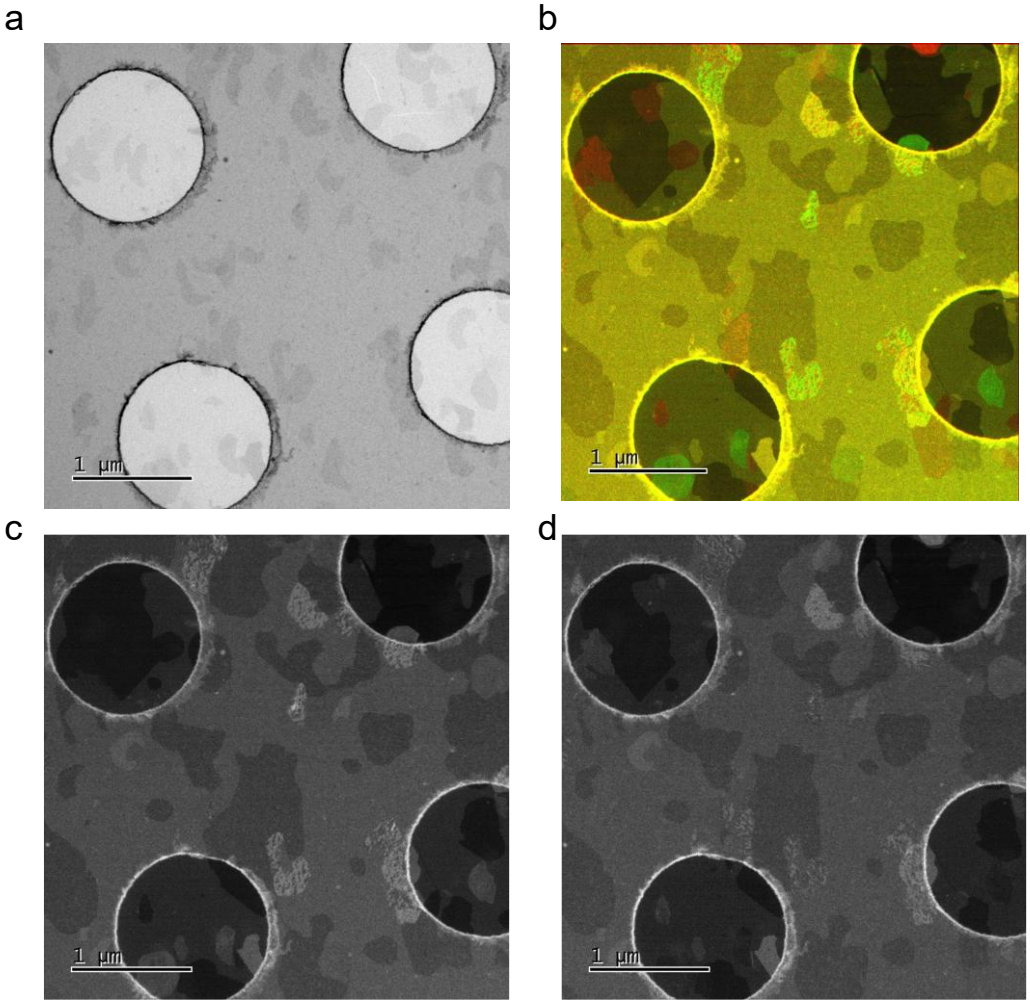

Figure S33. The TEM images of the MoS_2 monolayer deposited with 1.0 ppm of $Mo(CO)_6$ for 11 min, followed by 10 mins post-deposition annealing. A bright-field TEM image is shown in (a). A composite image with false colors (b) is composed using the dark-field TEM images (c, d). The dark, bright red and green areas on the composite images correspond to the misoriented domains. The misoriented domains can be distinguished from the secondary layer islands by comparing the composite and the bright-field image. Only secondary layer islands are visible on the bright-field image. The composite image was used in Figure 6a.

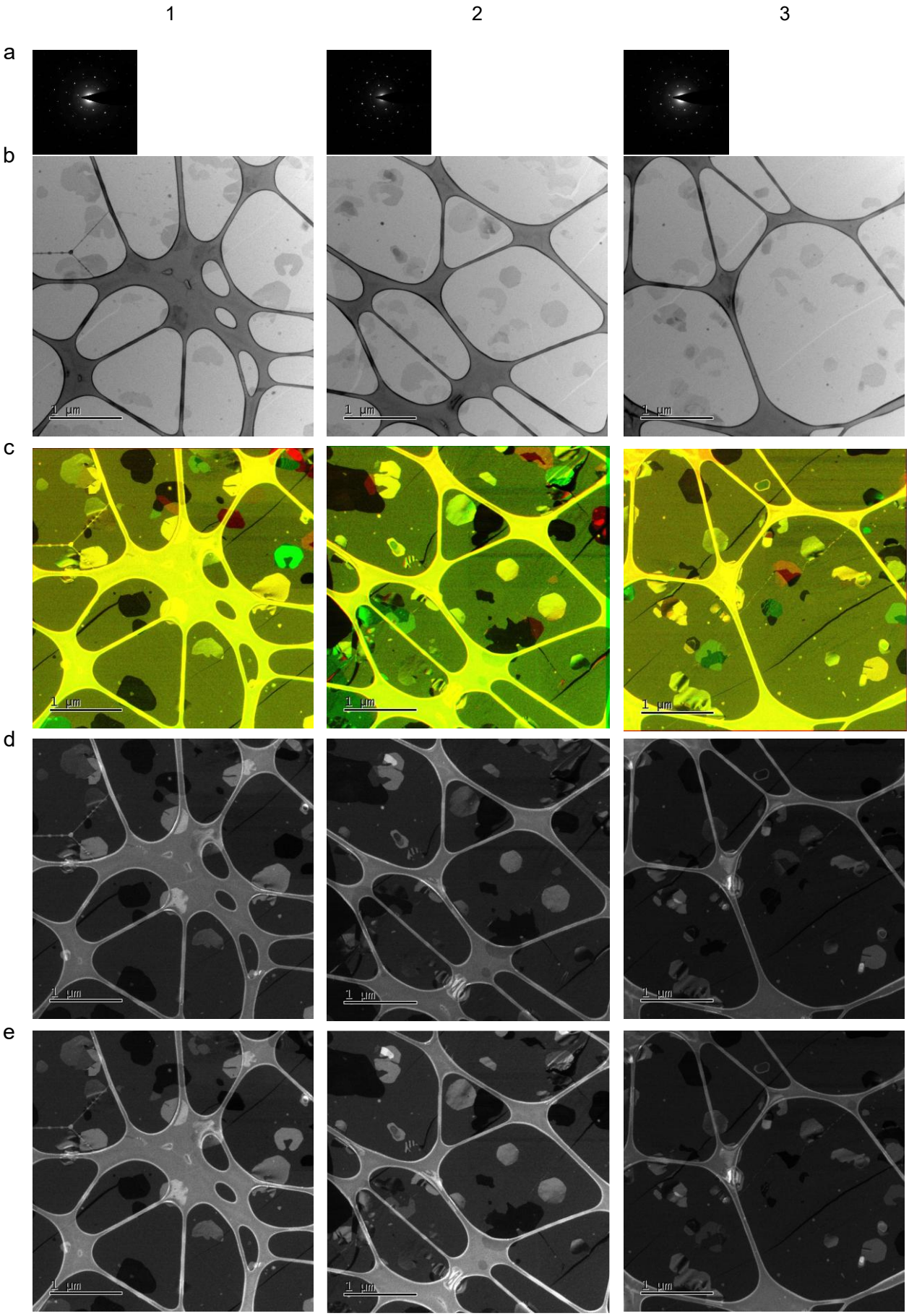

Figure S34. The TEM images from 3 regions for the MoS_2 monolayer deposited with 1.0 ppm of $Mo(CO)_6$ for 11 min, followed by 15 mins post-deposition annealing. The bright-field TEM images and the diffraction patterns are presented in (b) and (a), respectively. The composite images with false colors (c) are composed using the dark field

TEM images (d, e). The dark, bright red and green areas on the composite images correspond to the misoriented domains. The misoriented domains can be distinguished from the secondary layer islands by comparing the composite and the bright-field images. Only secondary layer islands are visible on the bright-field images. The composite image from region 1 was used in Figure 6b.

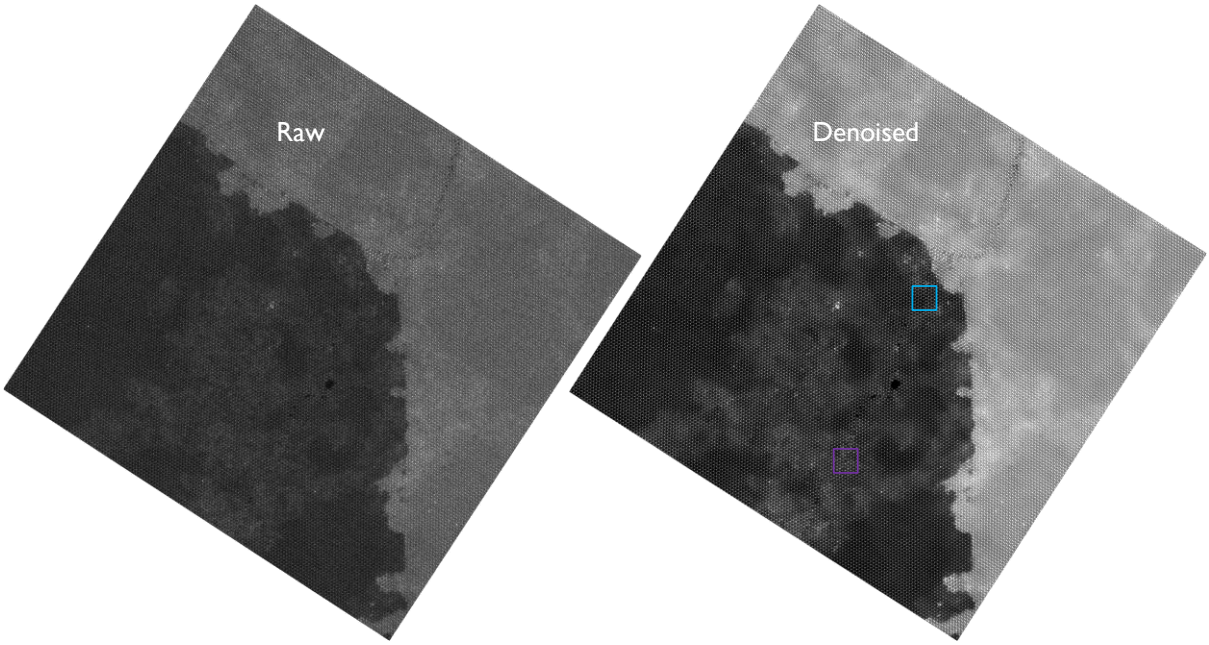

Figure S35. Large area HR-STEM images used in Figure 3e. Raw image was denoised using using trained deep learning model. [7] The blue square (top) highlights γ-grain boundary, the violet square (bottom) highlights β-grain boundary.

References

1. Palma, V. *et al.* H2 production by thermal decomposition of H2S in the presence of oxygen. *Int J Hydrogen Energy* **40**, 106–113 (2015).
2. Kang, K. *et al.* High-mobility three-atom-thick semiconducting films with wafer-scale homogeneity. *Nature* **520**, 656–660 (2015).
3. Voronenkov, V., Groven, B., Medina Silva, H., Morin, P. & De Gendt, S. Guiding Principles for the Design of a Chemical Vapor Deposition Process for Highly Crystalline Transition Metal Dichalcogenides. *Physica Status Solidi (A) Applications and Materials Science* **221**, (2024).
4. Chernov, A. A. Modern Crystallography III. **36**, (1984).
5. Kandybka, I. *et al.* Chemical Vapor Deposition of a Single-Crystalline MoS2 Monolayer through Anisotropic 2D Crystal Growth on Stepped Sapphire Surface. *ACS Nano* **18**, 3173–3186 (2024).
6. Rollett, A., Rohrer, G. S. & Humphreys, J. *Recrystallization and Related Annealing Phenomena*. *Recrystallization and Related Annealing Phenomena* (Elsevier, 2017). doi:10.1016/j.matchar.2020.110382.
7. Lobato, I., Friedrich, T. & Van Aert, S. Deep convolutional neural networks to restore single-shot electron microscopy images. *npj Computational Materials 2024 10:1* **10**, 1–19 (2024).